RESEARCH ARTICLE

Title: Mechanisms and purpose of lowered action potential firing threshold in fast-spiking interneurons in the human neocortex

Short title: *Lowered AP firing threshold in human pvalb neurons*
Field: Neuroscience

Authors

Emoke Bakos,[#1,2] Ádám Tiszlavicz,[#1] Viktor Szegedi,[1,2] Abdennour Douida,[1] Szabina Furdan,[1] Daphne Welter,[3] Jonathan Landry,[3] Balazs Bende,[4] Gabor Hutoczki,[5] Pal Barzo,[6] Gabor Tamas,[7] Vladimir Benes,[3] Attila Szucs,[8] Karri Lamsa*[1,2]

ORCID Identifiers:
Emoke Bakos: https://orcid.org/0009-0001-4790-4352
Adam Tiszlavicz: https://orcid.org/0009-0008-4830-0594
Karri Lamsa: https://orcid.org/0000-0002-4609-1337

Affiliations

[1]Hungarian Center of Excellence for Molecular Medicine Research Group for Human neuron physiology and therapy, Szeged, Hungary

[2]Department of Physiology, Anatomy and Neuroscience, University of Szeged, Szeged, Hungary

[3]European Molecular Biology Laboratory, Heidelberg, Germany

[4]Hungarian Centre of Excellence for Molecular Medicine Research Group for Translational Medicine Development, Szeged, Hungary

[5]Department of Neurosurgery, University of Debrecen Clinical Centre, Debrecen Hungary

[6]Department of Neurosurgery, University of Szeged, Szeged, Hungary

[7]ELKH-SZTE Research Group for Cortical Microcircuits, Department of Physiology, Anatomy and Neuroscience, University of Szeged, Szeged, Hungary

[8]Neuronal Cell Biology Research Group, Eötvös Loránd University, Budapest, Hungary

*correspondence to Karri Lamsa, email: klamsa@bio.u-szeged.hu, karri.lamsa@hcemm.eu
[#]These authors contributed equally to this work.

Abstract

The mammalian brain exhibits various interspecies differences. Microanatomical and molecular differences in homologous neurons between species are best characterized in the neocortical mantle, but the purpose of these differences remains poorly understood. We performed whole-cell microelectrode recordings and microanatomical and molecular analyses of human fast-spiking parvalbumin (pvalb)-expressing

interneurons in neocortical tissue resected during brain surgery. Fast-spiking interneurons exhibited a lower action potential (AP) firing threshold in humans than in mice. Compared with mouse neurons, human neurons displayed an elongated axon initial segment (AIS), and the human AIS was deficient in low-voltage activated inhibitory Kv1 potassium channels. Contrarily, Kv1 ion channels were prominent in mouse neurons. Computational fast-spiking interneuron model simulations revealed that human-type AIS lowers the AP threshold and shortens the time lag for AP generation. Thus, human AIS supports fast in–fast out electrical circuit function in human pvalb neurons, which have electrically slow membrane potential kinetics in somata.

Teaser: Fast-spiking neurons in the human neocortex have structural and molecular adaptations in the axon to shorten IN-OUT delay

MAIN TEXT

Introduction

All organs in the body are specialized during evolution to optimally serve animal life and vitality. The mammalian brain exhibits between-species differences in volume and the extent of cortical convolution, and in addition differences in the nerve cell microstructure and molecular content (*1, 2*). Although the brain consists of homologous neurons sharing similar localizations and developmental origins in different species, these neurons exhibit species-specific differentiation at the microscale level (*3-6*). The purpose of this neuronal specialization in different species is poorly understood (*7, 8*), although these adaptations are expected to optimize neural circuit function (*9*). Neuron types and their species diversity are best characterized in the neocortical mantle, which is the site of complex high-order brain functions (*1, 5, 6, 10-19*). The operation of the neocortex has been intensively studied concerning the cognitive and behavioral processes of the brain in both humans and experimental animals, and the latter have been used to elucidate the functions of different neuron types in these processes (*20-22*). However, studies utilizing resected human brain tissue reported various 'human-specific' transcriptomic and microstructural features in neocortical neurons (*7, 10, 11, 23-31*). Many of these variations are likely responsible for species-specific neuronal functions, but the connection between structure and function is poorly understood (*12, 16, 17, 19, 30, 32-34*).

The distinctive differences in homologous neurons between the rodent and human neocortex include their different electrical resistivity and differences in the membrane potential level required to trigger action potential (AP) (*25*). Excitatory pyramidal neurons in the human neocortex exhibit lower input resistance (Rin) and require larger membrane potential depolarization (i.e. have a higher AP firing threshold) to trigger AP than rodent neurons (*24, 29, 35*). Conversely, inhibitory interneurons in the human neocortex display greater electrical resistance and a lower AP firing threshold than their rodent counterparts (*26, 27*). There is indication in the literature that these interspecies distinctions apply to fast-spiking interneurons (*28, 31, 36*), the main inhibitory neuron population in the neocortex that is characterized by expression of *parvalbumin* (*PVALB*) gene encoding pvalb protein (*23*). Pvalb neurons in humans exhibit elevated electrical membrane resistance and therefore generate membrane potential (Vm) changes with reduced electric input currents (*28*). However, for the same reason Vm changes such as excitatory synaptic potentials leading to APs in

these cells are also elicited with a slower time course (*28, 31, 36-39*). The tardiness by which these Vm changes are elicited in human fast-spiking neurons compared with rodent fast-spiking neurons is counterintuitive because the rapid transformation of excitatory synaptic inputs to AP outputs (i.e., the input–output transformation) is characteristic of pvalb interneurons in the neocortex. These neurons are known as 'fast in–fast out' inhibitory circuits (*38, 40*). We hypothesize low AP threshold might occur together with the slow membrane potential kinetics in human pvalb neurons to speed up their input–output transformation.

In this study, electrophysiological whole-cell recordings in human and mouse *ex vivo* neocortical slices revealed an association between the slow Vm changes in soma and the lowered AP generation threshold in pvalb/*PVALB* interneurons. The lowered AP firing threshold in human cells was accompanied by structural and molecular specialization in the axon initial segment (AIS), a speciated feature in the axon to trigger APs (*41, 42*), which is elongated in human neurons and deficient in the inhibitory potassium channel Kv1. Fast-spiking interneuron simulation with the human-type AIS demonstrated that a lowered AP threshold reduces the time lag to evoke APs, which helps human pvalb neurons to operate as fast in–fast out electrical circuits despite the electrically slower soma (*43*).

Results

Pvalb interneurons in humans have lower AP firing threshold

We measured the AP firing threshold in 80 pvalb-expressing fast-spiking interneurons (*43*) in human neocortical tissue resected during deep brain surgery in 62 patients (Table S1). The cells were studied using the whole-cell clamp technique in layer 2/3 in acute brain slices sectioned from the frontal (n = 36), temporal (n = 20), and parietal or other neocortical regions (n = 24) in male (n = 29) and female patients (n = 33) aged 11–85 years. The neurons were filled with biocytin during recording and visualized with streptavidin–fluorophore *post hoc*. All cells were immunopositive for pvalb (n = 68, Fig. 1A1–3), or they expressed *PVALB* following nucleus harvesting and transcriptomic analysis of mRNA content using the patch-sequencing method (n = 12, Table S1). In parallel, we investigated pvalb-expressing interneurons in the mouse neocortex (n = 80).

We applied positive Vm steps (square-pulse current steps of incremental amplitude, 500 ms at 1 Hz) in cells current-clamped at −70 mV to identify the lowest threshold that triggered APs (Fig. 1B–C) (defined as the Vm at which the AP initial rise speed reaches 10 mV/ms; Fig. 1A1) (*31, 36, 44*). The AP firing threshold in human pvalb cells (median, −39.0 mV, interquartile range [IQR] = −44.8 to −34.7; n = 80 cells) was lower than that in mouse pvalb neurons (median, −33.4 mV; IQR = −35.9 to −28.4; n = 80 cells; $p < 0.001$, Student's *t*-test; Fig. 1D1–2).

We confirmed in human neurons that the AP firing threshold was similar in the frontal (−39.45 mV, IQR = −42.58 to −32.86 mV; n = 36 cells) and temporal cortices (−38.65 mV, IQR = −47.48 to −35.50 mV; n = 20 cells; $p = 0.179$, Student's *t*-test; Fig. 1E1). In addition, we calculated the average AP firing threshold per human subject, confirming that it did not depend on demographic characteristics. The pvalb cell firing

threshold was similar in male (−39.00 mV, IQR = −44.53 to −32.87 mV; n = 29) and female patients (−39.30 mV, IQR = −45.33 to −36.30 mV; n = 33; p = 0.682, Mann–Whitney U-test; Fig. 1E2), and no dependence on age was observed (r = −0.197; n = 60 patients; p = 0.135, Spearman's test; Fig. 1E3).

The results showed that human pvalb neurons have a lower AP firing threshold potential in response to excitation in the soma than mouse pvalb neurons.

The low AP threshold is associated with electrically slow somata in pvalb interneurons

Compared with mouse pvalb neurons, human pvalb neurons exhibited higher electrical resistance (i.e. input resistance, Rin) in soma, whereas no between-species difference in pvalb cell capacitance (Cm) was detected. We measured the average Rin and Cm in neurons in Vm steps of +5 to +10 mV (elicited by square pulse currents), which were excitatory but below the AP firing threshold (subthreshold) when applied at −70 mV (Fig. 2A1). Median Rin was 187.86 MΩ (IQR = 125.62–298.88) in human pvalb neurons (n = 50), versus 129.98 MΩ (IQR = 96.48–163.44) in mouse neurons (n = 40; p = 0.001, Mann–Whitney U-test; Fig. 2A2). Meanwhile, median Cm in the soma was 32.82 pF (IQR = 23.72–63.30) in humans (n = 50), compared with 31.39 pF (IQR = 23.25–41.85) in mice (n = 40; p = 0.620, Mann–Whitney U-test).

In addition, the time course of Vm changes (tau), measured systematically from the ascending phase in mV steps of +10 mV, was slower in human pvalb neurons than in mouse pvalb neurons (Fig. 2B1). The median electrical tau of the Vm step was 6.65 ms (IQR = 4.09–8.15) in humans (n = 50), versus 4.01 ms (IQR = 3.15–5.81) in mice (n = 40; p < 0.001, Mann–Whitney U-test; Fig. 2B2).

In mouse pvalb neurons, the membrane tau and cell Rin had a tight positive correlation (r = 0.625, p < 0.001; n = 40; Fig. 2C1), whereas no correlation was detected in human pvalb neurons (r = 0.114, p = 0.428; n = 50). Meanwhile, tau was similar in human pvalb neurons with high and low Rin (Fig. 2C2). However, in both species, a low AP firing threshold was associated with slow membrane tau (mice: r = −0.490, p = 0.001; n = 40; Fig. 2D1; humans: r = −0.331, p = 0.024; n = 50; Fig. 2D2). Data pooled from both species (Fig. 2D3) revealed a strong association between a low AP threshold and slow membrane tau (r = −0.575, p < 0.001, Spearman's correlation test; n = 90).

These results demonstrated that pvalb neurons with a slower time course for Vm changes in somata exhibit a lower AP firing threshold. This association is particularly strong when analyzing the human and mouse pvalb cells together.

The AIS is elongated in human pvalb neurons, and its localization along the axon is associated with the AP threshold

We visualized the AIS, an AP initiation site, of pvalb cells in the human and mouse neocortex because the AIS length and position along the axon can affect the AP threshold (*45*). We performed immunohistochemistry for beta-IV-spectrin, a cytoskeletal protein enriched in the AIS (*42*, *46*, *47*), and analyzed its immunofluorescence in three-dimensional confocal microscopic image stacks to

digitally measure the length of the AIS and its distance to the cell soma using a custom-made script. All cells were studied in layer 2/3 neocortex neurons, and their immunopositivity for pvalb was confirmed (Fig. 3A1).

Both human and mouse pvalb neurons exhibited cell-to-cell variation of the AIS length and its positioning along the axon (Fig. 3A2). The median distance from the AIS initiation site to the soma did not differ between human (4.12 µm, IQR = 2.95–5.28; n = 100 cells in 17 patients) and mouse neurons (3.77 µm, IQR = 2.69–4.68; n = 78 cells in 15 mice; p = 0.265). However, the median AIS length was greater in human cells (16.68 µm, IQR = 14.08–19.78) than in mouse cells (13.99 µm, IQR = 11.15–16.55; p < 0.001), and consequently, the AIS termination site was more distant from the soma in humans (21.01 µm, IQR = 17.60–24.66; 100 cells from 17 samples) than in mice (17.47 µm, IQR = 14.41–20.66 µm; 78 cells from 15 mice; p < 0.001, Mann–Whitney U-test; Fig. 3A2–3).

Next, we studied whether these AIS properties could explain the AP threshold difference between the two species. In electrophysiologically investigated and biocytin-filled neurons visualized with streptavidin–fluorophore and confirmed immunopositivity for pvalb, we visualized the AIS based on its positivity for beta-IV-spectrin and measured the AIS length and its distance from the soma along the axon. We compared the values against the AP firing threshold. From 28 human and 22 mouse cells recorded in the whole-cell clamp, the intact soma and full-length AIS were successfully recovered (demonstrated by beta-IV-spectrin immunofluorescence) in 13 human and 14 mouse neurons. Particular attention was paid to the acceptance of neurons for the analysis of biocytin-filled axons continuing beyond the distal end of the beta-IV-spectrin–visualized AIS to confirm that the AIS was entirely captured for measurement (Fig. 3B1). The distance from the initial part of the AIS to the soma in human pvalb neurons was 6.10 µm (IQR = 2.55–8.50; n = 13), versus 4.85 µm (IQR = 3.80–6.03; n = 14) in mouse neurons (p = 0.437; Fig. 3B2). The AIS was longer in human cells (17.60 µm, IQR = 14.65–20.20 µm) than in mouse cells (14.0 µm, IQR = 12.10–15.33; p = 0.004). Similarly, the distance from the AIS terminal site to the soma was longer in human neurons (23.60 µm, IQR = 20.85–25.75) than in mouse neurons (18.55 µm, IQR = 17.68–20.38; p < 0.001; Mann–Whitney U-test). The AIS properties are presented in Fig. 3B2. Neither of the AIS parameters was correlated with the AP firing threshold in human or mouse pvalb neurons. The correlation coefficient between the AIS proximal site distance and the AP firing threshold was 0.536 (p = 0.054) in human cells (n = 13) and −0.297 (p = 0.93) in mouse cells (n = 14). The AIS length and AP threshold were not significantly correlated in human (r = 0.203, p = 0.493) or mouse cells (r = 0.079, p = 0.773). The distance from the AIS termination site to the soma was not correlated with the AP threshold in human (r = −0.239, p = 0.414) or mouse cells (r = 0.024, p = 0.988, Spearman's correlation test). However, when AIS data from pvalb cells from both species were pooled together and tested, the AP threshold was correlated with the distance from the AIS initiation site to the soma (r = −0.478, p = 0.012; Fig. 3C1) and the distance from the termination site to the soma (r = −0.383, p = 0.0485) but not with AIS length (r = −0.1340, p = 0.516; Spearman's correlation test; Fig. 3C2–3).

The results illustrated that the AIS length and location along the axon differ between humans and mice, and that distal positioning of the AIS from soma associates with lowered AP threshold.

The axon diameter does not explain the interspecies difference in the AP firing threshold in pvalb neurons

We measured the axon diameter in biocytin-filled pvalb interneurons to study whether it is correlated with the AP firing threshold in cells because the axon caliber can regulate axon excitability (*48*). The diameter was measured using high-magnification fluorescence confocal microscopic images of biocytin-filled visualized neurons at five locations along the axon, including two measurement points before the AIS (pre-AIS) and three sites in the AIS, as illustrated in Fig. 4A1–3. The values represent the average per cell for the pre-AIS part of the axon and the part of the axon in the AIS. No difference in axon diameter was detected between human and mouse pvalb neurons in either in the pre-AIS (1.07 µm [IQR = 0.82–1.19] vs. 0.88 µm [IQR = 0.71–1.14]; p = 0.939) or AIS (0.83 µm [IQR = 0.70–0.96] vs. 0.69 µm [IQR = 0.64–0.74; p = 0.260; one-way ANOVA on ranks; Fig. 4B). In addition, the axon diameter in the pre-AIS and AIS was not correlated with the AP threshold in human (pre-AIS: r = 0.245, p = 0.429; AIS: r = 0.392, p = 0.197; n = 13) or mouse neurons (pre-AIS: r = 0.091, p = 0.766; AIS: r = 0.056, p = 0.852; n = 12). Combining all cells from both species, the axon width and AP threshold were not associated in either the pre-AIS (r = 0.137, p = 0.518; Fig. 4C1) or AIS (r = −0.036, p = 0.866; Spearman's correlation test; Fig. 4C2). These results show that the axon diameter is unlikely to explain the interspecies difference in the AP threshold in pvalb neurons.

Nav1.6 channels are robustly and uniformly distributed in the AIS in both human and mouse pvalb neurons

We studied the immunoreactivity for the low-voltage gated sodium channel Nav1.6 in the AIS of pvalb neurons (Fig. 5A) because the density and spatial distribution of Nav1.6 channels in the AIS can regulate the threshold of AP generation (*49, 50*). Nav1.6 channels can be concentrated at the distal end of the AIS to reduce the AP firing threshold (*48, 49, 51, 52*), or they may be evenly distributed along the AIS. In parallel with pvalb and beta-IV-spectrin immunofluorescence analyses in human and mouse neocortex layer 2/3, we studied the Nav1.6 immunofluorescence intensity in three-dimensional confocal microscopic image stacks along the axon to investigate whether the localization pattern of the channels in the AIS differed between the species (Fig. 5B). We measured the immunofluorescence intensity along the axon from the soma to beyond the AIS termination site. Triple immunofluorescence analysis along the axon uncovered a robust immunofluorescence signal for Nav1.6 in human and mouse neurons with a uniform distribution along the AIS, as presented in Fig. 51C (*51*). To further analyze the immunofluorescence data, the signal values were averaged for the proximal part of the axon from the soma to the initiation site of the AIS (pre-AIS), the AIS, which is the part of the axon exhibiting beta-IV-spectrin immunofluorescence, and the axon beyond the AIS (post-AIS; Fig. 5C1). The Nav1.6 immunofluorescence intensity average in the AIS (F_{AIS}) in human cells was 1.94-fold (IQR = 1.75–3.04) higher than that in the pre-AIS axon segment (F_{pre}, n = 21). In mouse pvalb cells, Nav1.6 F_{AIS} was 1.86-fold (IQR = 1.61–2.25) higher than F_{pre} (p = 0.181, Mann–Whitney U-test; n = 26; Fig. 5C2). The results indicate similar Nav1.6 density and localization pattern in the AIS in human and mouse pvalb neurons.

Human pvalb neurons exhibit low level of Kv1.1 and Kv1.2 channels in the AIS

We similarly studied the immunofluorescence of Kv1.1 and Kv1.2 potassium channels, which are key inhibitory potassium channels controlling the AP threshold in the AIS in many neurons (*53, 54*) (Fig. 6A1–2). In particular, Kv1.1 channels are clustered in the AIS in rodent pvalb neurons (*55*), in which their presence as low-threshold inhibitory channels increases the AP firing threshold (*53, 56*). We compared the immunofluorescence signal for Kv1.1 and Kv1.2 channels in the AIS in human and mouse pvalb neurons in identical separate triple immunoreaction studies.

Triple immunoreactions for Kv1.1, pvalb, and beta-IV-spectrin showed a robust Kv1.1 signal systematically in the AIS in mouse pvalb cells, as previously reported (*53*), but in human pvalb cells, the Kv1.1 immunoreaction reaction was weak or absent in the AIS despite the strong immunoreaction in pvalb-immunonegative neurons in the same immunostained sections (Fig. 6A1–2). Figure 6A3–4 presents sample pvalb neurons in human and mouse with Kv1.1 immunofluorescence analysis along the axon. For Kv1.1 channels, F_{AIS} was 1.15-fold (IQR = 1.07–1.32) higher than F_{pre} in human pvalb neurons (n = 33), whereas in mouse pvalb neurons, F_{AIS} was 1.39-fold (IQR = 1.21–1.67) higher than F_{pre} (n = 31; Fig. 6A5). The F_{AIS}/F_{pre} ratio for Kv1.1 was significantly higher in mice compared to humans ($p < 0.001$, Mann–Whitney U-test; Fig. 6A6) indicating stronger aggregation of Kv1.1 channels in the AIS in mice.

The AIS expresses Kv1.2 potassium channels in many neurons in rodents (*57*). However, the immunofluorescence signal for Kv1.2 channels in the AIS was absent in both human and mouse pvalb neurons (Fig. 6B1–2), although a robust Kv1.2 immunoreaction was observed in non-pvalb neuron dendrites and somata in the same immunostained sections (Fig. 6B1–2). Systematic line analysis of the fluorescence intensity along the axon (Fig. 6B3–4) illustrated that the F_{AIS}/F_{pre} ratio for Kv1.2 immunofluorescence was 1.05 (IQR = 0.97–1.14; n = 64) in humans and 1.02 (IQR = 0.95–1.11; n = 33) in mouse pvalb cells (Fig. 6B5). The Kv1.2 F_{AIS}/F_{pre} ratio did not differ between humans and mice ($p = 0.206$, Mann–Whitney U-test; Fig. 6B6). The results indicate low level of Kv1.2 potassium channels in the AIS in both species.

Pvalb neurons in humans lack mRNA for *KCNA1* encoding Kv1.1 channels

We utilized the patch-sequencing method to measure the mRNA levels of key low-threshold ion channels responsible for the AP firing threshold, including Kv1.1 and Kv1.2, in pvalb neurons (*44, 51, 53-55, 58*). We studied fast-spiking interneurons electrophysiologically in both species using the whole-cell clamp technique and harvested cell nuclei for mRNA transcriptomic analysis (*59, 60*). The mRNA quantification uncovered mRNA for 6784 genes (IQR = 4872–7399) in humans (n = 21) and 3617 genes (IQR = 3173–4305) in mice (n = 16; Fig. 7A1–2). The transcriptomic data of individual cells were uploaded to the Allen Institute neuron type identification server with an algorithm categorizing neocortex layer 2/3 neuron types by the genes expressed (https://knowledge.brain-map.org/mapmycells/process/), enabling human and mouse pvalb neuron identification also in cells with undetectable *PVALB* mRNA expression but positive expression for gene combinations indicating the pvalb cell subtype (Fig. S1). Using the same criteria for pvalb cell subtypes, we identified 21 and 16 pvalb neurons in our human and mouse dataset, respectively. The cells were further analyzed for *KCNA1*, *KCNA2*, *KCNC1*, *KCNC2*, *KCND1* and

SCN8A expression, as well as the expression of housekeeping genes (*ACTB*, *GAPDH*, and *SLC8A1*; Fig. 7A1–2).

The transcriptomic analysis illustrated that human pvalb neurons lacked, or had undetectable, mRNA expression for *KCNA1* in all 21 cells, whereas *KCNA1* was robustly expressed in 7 of 16 mouse pvalb neurons. The mRNA level heatmap in Fig. 7A1 presents the gene expression (as transcripts per million [TPM]) for individual pvalb neurons in humans and mice. *PVALB* mRNA expression was undetectable in 10 of 21 human neurons and 6 of 16 mouse neurons, in line with the Allen Institute open access database results for layer 2/3 pvalb neurons, demonstrating that *PVALB* mRNA expression is very low in certain pvalb neurons (Fig. S1). A comparison of *KCNA1* mRNA expression between human ($n = 21$) and mouse cells ($n = 16$) revealed a significant difference ($p = 0.0016$, one-way MANOVA with the *post hoc* Bonferroni test). In addition, categorical comparisons (positive or negative mRNA expression) illustrated that *KCNA1* expression in pvalb neurons significantly differed between mice and humans ($p < 0.001$, chi-squared test after Benjamini–Hochberg adjustment at the 5% significance level; Fig. 7B).

Cells in both species displayed robust mRNA expression for *KCNA2* without an interspecies difference ($p = 0.970$). In addition, cells in both species had equally strong mRNA expression of *KCNC1* and *KCNC2* ($p = 0.878$ and $p = 0.053$, respectively), which respectively encode the Kv.3.1 and Kv3.2 channels characteristics of pvalb interneurons (*43, 61*), and they similarly exhibited low or absent expression of *KCND1* encoding Kv4.1 potassium channels (*62*) ($p = 0.541$). Both human and mouse pvalb cells strongly expressed mRNA for *SCN8A* encoding Nav1.6 sodium channels ($p = 0.086$). In addition, all cells had prominent mRNA levels for *ACTB* and *GAPDH* (Fig. 7A1). Interestingly, the mRNA expression of *SLC6A1* encoding gamma-aminobutyric acid (GABA) transporter 1 was lower in human neurons than in mouse neurons ($p = 0.002$). Neither the comparison of TPM values nor categorical mRNA expression uncovered a significant difference between human and mouse pvalb neurons for the mRNAs of other genes. The results were in line with the averaged mRNA levels in pvalb neuron types from the Allen Institute open access database (Fig. S1).

We tested the association of the pooled mRNA values (TPM) of *KCNA1* and *KCNA2* with the AP threshold in the patch-sequenced neurons (Fig. 7B), and no association was observed for either gene with the AP threshold in humans ($r = 0.041$, $p = 0.861$; $n = 20$) or mice ($r = 0.236$, $p = 0.388$; $n = 15$). Similarly, no association was detected when cells from both species were pooled together and tested ($r = 0.175$, $p = 0.312$, Spearman's correlation test; $n = 35$).

Results show absence of *KCNA1* expression in human but not in mouse pvalb neurons, and no difference between species in *KCNA2* expression.

Fast-spiking neuron computational model with a human-type AIS revealed a lowered firing threshold and a shortened time lag to AP generation

We established a computational single-cell model with cable properties in axon (and dendrites) featuring an AIS mimicking the human pvalb cell electrical properties measured in actual neurons. We simulated the effects of species-associated AIS

parameters, particularly the AIS length and AIS Kv1 channel content, on the AP firing threshold and time lag between AP generation and excitation in the soma. The intrinsic electrical properties of the model cell were adjusted to mimic the Vm waveforms and AP firing threshold of human pvalb cells during the voltage steps, as illustrated in Fig. 8A1–2. The model cell replicated a whole-cell recorded human pvalb cell (code h7, see Table S1) possessing Hodgin–Huxley type AP with voltage-sensitive axonal low-threshold Na current (mimicking Nav1.6 in the AIS), high-threshold Na current (Nav1.2 at the soma and proximal dendrite), and K current (mimicking Kv3.1 and Kv3.2 in the AIS, soma, and dendrite). It had voltage-insensitive K leak current, M-type K current, and Kir-type K current at the soma and dendrite (*63*), and the hyperpolarization-activated non-specific cation current Ih in the soma and dendritic compartments (*28*). In addition, we applied variable Kv1 activity in the AIS. In standard conditions, the model cell AIS length was 20 µm, and initiation distance to the soma was 10 µm, and the AP firing threshold was −43 mV.

First, we simulated the AP firing threshold by altering the AIS lengths (10–30 µm) mimicking the range discovered in the anatomical investigation of real-life pvalb neurons. Increasing the AIS length linearly increased the Nav1.6 and Kv1channel activity in the AIS (channel conductances gNav1.6 and gKv.1 were fixed at 20 nS/µm^2 for both channels). Axons had a diameter of 0.8 µm and longitudinal resistance (Ra) of 0.9 MΩ·µm. AIS elongation from 10 µm to 20 and 30 µm reduced the AP firing threshold (elicited by a 250-ms square-pulse current in the soma at −70 mV) in the model cell from −36.8 mV to −42.3 and −45.2 mV, respectively (Fig. 8B1–2) demonstrating that the pvalb cell AIS length range observed in this study can markedly alter the AP firing threshold.

In the second simulation, we changed the activity of Kv1 channels in the AIS while fixing the AIS length (20 µm) and location along the axon (10 µm from the soma, Ra = 0.9 MΩ·µm), as well as the gNav1.6 density (20 nS/µm^2). We simulated AP generation by depolarizing the voltage steps in the cell to define the AP firing threshold as previously described. When gKv1 was increased from 0 nS/µm^2 to 5, 10, and 15 nS/µm^2 in the AIS (Fig. 8C1–2), the AP firing threshold increased from −45.3 mV to −44.2, −42.4, and −41.6 mV, respectively (Fig. 8D). This simulation illustrated that increasing the Kv1 activity in the AIS without changing AIS geometry increases the AP firing threshold.

In addition, we repeated the simulation using parameters featuring cell-to-cell variability in both species but no difference between the species. Simulation with the model (AIS length = 20 µm; gNav1.6 and gKv1 densities = 20 nS/µm^2) while varying the AIS initial site distance to the soma over a range observed in the anatomical study (0 or 10 µm) revealed a moderately lowered AP firing threshold with a distance of 10 µm to the soma (−43.2 mV) compared with 0 µm (−41.5 mV; Fig. S2A). We also simulated the effect of axon diameter variation (0.6–0.9 µm) on the AP threshold through changes in Ra (0.8–1.1 MΩ·µm) and alteration of the axon extracellular membrane surface area (estimated as diameter × π with gNav1.6 and gKv1 of 20 nS/µm^2). The simulations demonstrated that the AP firing threshold was lowest (−44.7 mV) in the model cell with the narrowest axon diameter (0.6 µm) and highest Ra (1.1 M MΩ·µm). The highest AP threshold (−42.2 mV) was observed with the largest axon diameter (0.9 µm) and lowest Ra (0.8 MΩ·µm). The results demonstrated that changing Ra without altering the axon surface area changes the AP firing

threshold to less than 1 mV. Similarly, a theoretical condition in which Ra remains unchanged but the axon diameter changes, thereby increasing the ion channel activity, changes the AP threshold maximally 2 mV. Notably, by increasing the axon diameter over a range observed in the anatomical study, lowering Ra while increasing Nav1.6 and Kv1 activity, increased the AP firing threshold. These conditions and their interrelationships are demonstrated in the heatmap in Fig. S2B.

Finally, we used the model cell to understand the effects of the AP firing threshold, as altered by the AIS length and Kv1 content, on the time lag in pvalb neurons to generate AP in response to synaptic excitation in the soma. The simulation aimed to answer why human pvalb neurons, compared with mouse pvalb neurons, with a slower somatic membrane tau (Fig. 8E1) but lower AP firing threshold (Fig. 8E2) can fire APs with an equal or shorter time lag to the fixed-amplitude excitatory current in the soma (Fig. 8E3–4) (*38*). In the model neuron, we generated an excitatory postsynaptic current (EPSC) in the soma at −70 mV and incrementally increased its peak amplitude to evoke a gradually increasing excitatory postsynaptic potential (EPSP) that finally reached the AP firing threshold (*28*). The EPSC was generated with peak conductance from 6 to 11 nS with an incremental step of 0.25 nS, reaching the AP firing threshold with the human-type and mouse-type AIS with EPSC conductance values of 6.75 and 8.5 nS, respectively (Fig. 8F1–3). Shifting from 'the mouse-type AIS' (Kv1 density 20 nS/μm^2, AIS length 10 μm) to 'the human-type AIS' (Kv1 density 0 nS/μm^2, AIS length 30 μm) shortened the time lag for AP generation compared with the EPSP-AP time lag generated with a fixed EPSC strength (Fig. 8F2–3). The EPSP-AP time lag simulation with varying AIS length and differing Kv1 content in the AIS is illustrated in the heatmap in Fig. 8G. The simulation identified minimum and maximum time lags for AP generation of 4.8 and 7.8 ms, respectively, for a fixed EPSC strength (8.5 nS, the AP firing threshold in mouse cell) in the model cell.

These experiments demonstrated that the lowered AP firing threshold for the human AIS compared with the mouse AIS in pvalb cells was associated with a shorter AP generation time lag by the synaptic current in the soma.

Discussion

Species-specific features in organs, tissues, and cells have evolved in response to selection pressure during species phylogeny in evolution (*8, 64, 65*). Consequently, homologous cell types (i.e., neurons expressing the same common cell-type specific marker genes) are largely similar across different mammalian species while also exhibiting interspecies differences, which represent adaptations to gain functional advantages (*4, 66-69*). Our findings suggested that fast-spiking pvalb neurons in the neocortex of the human brain evolved with a lowered AP firing threshold to facilitate AP generation and their function as fast in–fast out circuits. This increased speed of the fast-spiking neuron input-to-output transformation is important to human cells, which have an electrically slow soma compared to rodent neurons. Correlative evidence together with model cell simulations indicated that the lowered AP threshold in human pvalb neurons emerged from the elongated AIS and the reduced Kv1 inhibitory potassium channel content of the AIS.

A low AP firing threshold helps electrically slower human interneurons to function as 'fast in–fast out' circuits

A short lag in AP generation in response to excitatory synaptic input (i.e., input–output transformation) is a hallmark of fast-spiking pvalb interneurons in the cortex across mammalian species (*40, 43*). These neurons form the largest cortical inhibitory neuron population (*6, 70, 71*), and they orchestrate the firing activity of other various neuron types through rapid and time-precise synaptic inhibition (*43*). In many pvalb neurons in the human neocortex, rapid signal transformation would be challenging because of the slower electrical time course for Vm changes in somata. However, the lowered AP firing threshold provides a compensatory mechanism to shorten the input–output transformation time lag in these neurons. This helps securing the archetypical fast in–fast out function of pvalb neurons in the human neocortex, as we demonstrated using a computational model.

The deceleration of the inhibitory circuits' signaling speed in the human neocortex would be deleterious, as such changes have been linked to reduced computational speed of the neuronal circuits and cognitive deficits in the brain cortex in theoretical models and real-life animal experiments (*40, 72-75*). Therefore, fast-spiking interneurons in the human neocortex have different evolutionary adaptations that support their rapid electrical input–output signal transformation. These neurons exhibit a simplified geometry of the dendritic tree to facilitate the propagation of synaptic potentials from distal dendrites to somata (*2, 31*). In addition, human pvalb neurons show a higher number of voltage-sensitive excitatory cation channels in the proximal dendrites and soma plasma membrane to shorten the membrane potential kinetics (*28*). In addition, we observed the adaptation in pvalb neuron AP generation in the soma. It is likely that at least some of these adaptations occur generally among primate pvalb neurons, as cells in the macaque monkey neocortex also exhibit a slower time course of Vm changes and a lowered AP threshold compared to rodent neurons (*36*).

Why do human pvalb neurons have electrically slower somata than rodent neurons?

The electrically slower soma membrane in human pvalb neurons mechanistically emerged from the increased cell Rin caused by low transmembrane ion leakage. This conclusion is supported by results illustrated that the cell Cm measured in the soma, a parameter with Rin to define the somatic membrane tau, is similar in primate and rodent fast-spiking neurons (*36, 37*). In mouse pvalb neurons, the soma membrane tau is tightly associated with cell Rin, but these two factors are not associated in human neurons. This indicates that human pvalb cells exhibit highly variable cell-to-cell ion channel activity at the plasma membrane (and hence variable electrical resistivity per plasma membrane area) to determine the plasma membrane ion leak (*76*).

It is unknown why the high Rin evolved in human pvalb neurons because it basically is unfavorable for their fast in–fast out operation. One explanation is that evolutionary pressure pushed pvalb interneurons to generate Vm changes with reduced electric currents and thus with reduced transmembrane ion fluxes to save metabolic energy costs in ion transportation and ion gradient maintenance (*77, 78*), as fast-spiking interneurons are high energy-consuming neurons (*79-81*), and their energy demand is apparently pronounced in the human brain because of the increased proportional content of interneurons in the cortex compared with that in rodents (*14,*

82, 83). However, the development of a plasma membrane with increased electrical resistivity in human pvalb neurons also apparently required AP threshold adjustment in these neurons to secure the maintenance of their rapid electrical input–output transformation.

Mechanisms behind the lowered firing threshold in human fast-spiking neurons

Human pvalb neurons have a longer AIS on average than their mouse counterparts, and computational simulation demonstrated that the AIS length is a powerful modulator of the firing threshold in the range observed in actual pvalb neurons. The AIS length likely contributes to the AP threshold variability in individual pvalb cells in both species and additionally explains at least some of the interspecies difference. The increased length of the AIS lowers the AP threshold by increasing total number of Na channels in the initial segment (*41, 48*), and the effect is particularly effective in human neurons AIS with low inhibitory Kv1 channel content. In addition, an increase in AIS length is more effective in lowering the AP threshold than axon diameter expansion, although both variables increase the number of ion channels in the plasma membrane in the AIS. The increased number of ion channels with axon diameter extension was not efficient in lowering the AP threshold because it simultaneously reduced Ra, which shifted the AP threshold in the opposite direction (*48*).

Immunofluorescence analysis revealed a deficiency in Kv1.1 channels in pvalb neurons in the human neocortex, and *KCNA1* expression was absent in all human pvalb neurons, although it was robustly present in many mouse cells. These results were in line with those in the Allen Institute open database of transcriptomics of averaged mRNA levels in human and mouse pvalb neuron subtypes, as also summarized in Fig. S2. Although Kv1.2 channels are similarly expressed in human and mouse pvalb neurons, the immunohistochemical results showed they are weakly present in the AIS in both species. However, the mRNA levels of the pooled Kv1.1 and Kv1.2 mRNAs in pvalb neurons were not correlated with the firing threshold of individual cells. Future studies with larger datasets could further elucidate this relationship.

Alterations in the composition of voltage-gated K channels in the AIS coincide with elongation of the AIS in certain neurons in rodents to enhance neuronal excitability (*45*). Human pvalb neurons have taken advantage of this rule by using both geometric and ion channel activity mechanisms to lower their AP generation threshold.

Mechanisms underlying the cell-to-cell variability of the AP threshold without between-species differences

The distance from the AIS initiation site to the soma also affects the AP firing threshold (*42, 48*), and it likely contributes to the cell-to-cell variability in pvalb neurons in both species, as also indicated by recordings in real-life neurons and simulations with the model cell. However, it does not explain interspecies difference in the AP threshold in pvalb neurons given that the distance from the AIS initial site to the soma did not differ between the humans and mice.

In addition, although the axon diameter also contributes the AP threshold (*48*) and it possibly plays a role in cell-to-cell AP threshold variability in pvalb neurons, the current results indicated that the lowered AP threshold in human neurons was not generated by the axon diameter. Any Ra decrease in axons, which is expected to occur

with axon diameter increases, in fact increases the AP threshold in pvalb interneurons. Given the existence of evolutionary pressure to lower the AP threshold in human neurons, it is logical that the human pvalb interneuron axon diameter is not markedly larger than that in mouse cells because diameter enlargement might counteract the AP threshold lowering.

The AIS is not a static cellular microdomain (*84*), and the cell-to-cell variability in the AIS observed in pvalb in both species is established through plasticity processes (*85*), offering a tool that allows the brain to adapt to environmental changes, learn, and repair itself. Whether these plasticity processes differ between humans and experimental animals is unknown.

Limitations of the study

Limited availability of biotechnological tools to selectively and rapidly modify gene expression, and hence the AIS ion channel content and microstructure in genetically specified neuron types, such as pvalb neurons, in human brain slices restricted the experimental design of this study. In the future, availability of these techniques in human brain slices will help to establish a more detailed picture on the 'human type AIS' and its role in neuron function.

Materials and Methods

Ethics statement and licenses

All procedures were approved by the University of Szeged Ethics Committee and the Regional Human Investigation Review Board (ref. 75/2014) and conducted in accordance with the tenets of the Declaration of Helsinki. Written informed consent for studies on excised human cortical tissue was obtained from all patients before surgery. Tissue obtained from underage patients was provided with agreement from a parent or guardian.

Human brain slices

Neocortical slices were prepared from samples of the frontal, temporal, or other cortices removed for the surgical treatment of deep-brain targets. The patient age range was 11–85 years, and samples were acquired from both the left and right hemispheres of male and female patients (Table S1). Anesthesia was induced with intravenous midazolam (0.03 mg/kg) and fentanyl (1–2 μg/kg) following a bolus intravenous injection of propofol (1–2 mg/kg). The patients also received 0.5 mg/kg rocuronium to facilitate endotracheal intubation. Patients were ventilated with a 1:2 O_2/N_2O mixture during surgery, and anesthesia was maintained with sevoflurane. Following surgery, the resected tissue blocks were immediately immersed in an ice-cold solution containing (in mM) 130 NaCl, 3.5 KCl, 1 NaH_2PO_4, 24 $NaHCO_3$, 1 $CaCl_2$, 3 $MgSO_4$, and 10 d-(+)-glucose aerated with 95% O_2/5% CO_2 within a glass container. The container was then placed on ice inside a thermally isolated box and (within 20 min) transported from the operating room to the electrophysiology laboratory with continuous 95% O_2/5% CO_2 aeration. Slices (350 μm thick) were prepared from the tissue block using a vibrating blade microtome (Microm HM 650 V, Campden Instruments Ltd., Leics, UK) and then incubated at 22–24°C for 1 h in slicing solution. The slicing solution was gradually replaced with a recording solution (180 mL) using a pump (6 mL/min). The contents of the recording solution were identical to those of the slicing solution except that it contained 3 mM $CaCl_2$ and 1 mM $MgSO_4$.

Mouse brain slices

Transversal slices (350 μm) were prepared from the somatosensory and frontal cortices of 5–7-week-old heterozygous B6.129P2-Pvalbtm1(cre)Arbr/J mice (stock 017320, B6 PVcre line, Jackson Laboratory, Bar Harbor, ME, USA) crossed with the Ai9 reporter line to express the tdTomato fluorophore in pvalb GABAergic neurons to assist in cell selection. Cell identity was tentatively confirmed electrophysiologically by fast spike kinetics and high-frequency non-accommodating firing in response to 500-ms suprathreshold depolarizing pulses (*38*).

Electrophysiological recordings and data analysis

Recordings were performed in a submerged chamber perfused at 8 mL/min with the recording solution maintained at 36–37°C. The cells were patched under visual guidance using infrared differential interference contrast video microscopy and a water-immersion ×20 objective with an additional zoom (up to ×4) and appropriate dichroic mirror and filter (Cy3) for mouse tissue TdTomato signal epifuorescence. All experiments were performed within 30 min from entering the whole-cell mode. Micropipettes (5–8 MΩ) were filled with an intracellular solution containing (in mM) 126 K-gluconate, 8 NaCl, 4 ATP-Mg, 0.3 Na_2-GTP, 10 HEPES, and 10 phosphocreatine (pH 7.0–7.2; 300 mOsm) supplemented with 0.3% (w/v) biocytin for subsequent staining with Alexa 488-conjugated streptavidin. Recordings were performed with a Multiclamp 700B amplifier (Axon Instruments, Scottsdale, AZ, USA) and low-pass–filtered at a cutoff frequency of 6–8 kHz (Bessel filter). The series resistance and pipette capacitance were compensated in the current–clamp mode. The Vm values were not corrected for the liquid junction potential error. Somatic tau values were measured in the current–clamp mode for depolarizing (+10 mV) Vm steps (250–500 ms) from −70 mV. The AP firing threshold was measured in the dV/dt per Vm phase plots as the Vm at which the AP initial rise speed reaches 10 mV/ms (*31*, *44*). All parameters were measured from at least five traces. Data were acquired using Clampex software (Axon Instruments), digitized at 35–50 kHz, and analyzed offline using pClamp (version 10.5, Axon Instruments), Spike2 (version 8.1, Cambridge Electronic Design, Milton, UK), OriginPro (version 9.5, OriginLab Corporation, Northampton, MA, USA), and SigmaPlot (version 14, Grafiti, Palo Alto, CA, USA).

Tissue fixation and cell visualization

Cells filled with biocytin from whole-cell patch-clamp recording were visualized using either Alexa 488-conjugated streptavidin (1:1000, Jackson ImmunoResearch, West Grove, PA, USA) or Cy3-conjugated streptavidin (1:1000, Jackson ImmunoResearch). After recording, the slices were immediately fixed in a solution containing 4% paraformaldehyde and 15% picric acid in 0.1 M phosphate buffer (PB; pH 7.4) at 4°C for at least 12 h and then stored at 4°C in 0.1 M PB containing 0.05% sodium azide as a preservative. All slices were embedded in 20% gelatin and further cut into 50 μm-thick sections in ice-cold PB using a vibratome (VT1000S, Leica Microsystems, Wetzlar, Germany). After sectioning, sections were rinsed in 0.1 M PB (3 × 10 min), cryoprotected in 10%–20% sucrose solution in 0.1 M PB, flash-frozen in liquid nitrogen, and thawed in 0.1 M PB. Sliced sections were then incubated in 0.1 M Tris-buffered saline (TBS; pH 7.4) containing fluorophore-conjugated streptavidin for 2 h 30 min at 22–24°C. After washing with 0.1 M PB (3 × 10 min), the sections were covered in Vectashield mounting medium (Vector Laboratories, Burlingame, CA, USA), placed under coverslips, and examined

under an epifluorescence microscope at ×20–60 magnification (Leica DM 5000 B, Milton Keynes, UK). Sections used for single-cell reconstruction were further incubated in a solution of conjugated avidin–biotin horseradish peroxidase (1:300; Vector Labs) in TBS (pH 7.4) at 4°C overnight. The enzyme reaction was visualized by the glucose oxidase–DAB–nickel method using 3′3-diaminobenzidine tetrahydrochloride (0.05%) as the chromogen and 0.01% H_2O_2 as the oxidant. Sections were further treated with 1% OsO_4 in 0.1 M PB. After several washes in distilled water, the sections were stained with 1% uranyl acetate, dehydrated in an ascending series of ethanol concentrations, infiltrated with epoxy resin (Durcupan, Merck kft., Budapest, Hungary) overnight, and embedded on glass slides. Light microscopic reconstructions were conducted using the Neurolucida system (MBF Bioscience, Williston, VT, USA) with a ×100 objective (Olympus BX51, Olympus UPlanFI, Olympus, Tokyo, Japan). Images were collapsed in the z-axis for illustration.

Immunohistochemistry

Free-floating sections were washed three times in TBS containing 0.3% Triton-X (TBST) for 1 h at 20-24°C . They were then moved to a blocking solution consisting of 20% horse serum in TBST. The sections were treated with 1 mg/mL pepsin (catalog #S3002; Dako, Glostrup, Denmark) in 1 M HCl with 0.1 M PB at 37°C for 5-6 min and then washed in 0.1 M PB. All sections were incubated in primary antibodies diluted in TBST over three nights at 4°C followed by the appropriate fluorochrome-conjugated secondary antibody solution (2% blocking serum in TBST) overnight at 4°C. The sections were first washed in TBST (thrice for 15 min each), washed in 0.1 M PB (twice for 10 min each), and finally mounted on glass slides with Vectashield mounting medium (Vector Laboratories, Burlingame, CA, USA). For immunolabeling, the following primary antibodies were used: goat anti-pvalb (1:1000, PVG-213, Swant, Burgdorf, Switzerland); mouse anti-spectrin beta-4 (1:100, Invitrogen, Thermo Fisher Scientific, Waltham, MA, USA), rabbit anti-Nav1.6 (SCN8A, 1:300, Alomone Labs, Jerusalem, Israel); rabbit anti-Kv1.1 (KCNA1, 1:100, Alomone Labs), and rabbit anti-Kv1.2 (KCNA2 APC-010, 1:100, Alomone Labs). The immunolabeling was visualized for confocal microscopy using the following secondary antibodies: DAM Alexa 488-conjugated donkey anti-mouse (1:400, Jackson ImmunoResearch), DARb Cy3-conjugated donkey anti-rabbit (1:400, Jackson ImmunoResearch), and DaGt A647-conjugated donkey anti-goat (1:200, Thermo Fisher Scientific). The immunoreactions were evaluated using an epifluorescence microscope with a quasiconfocal option (Zeiss ApoTome 2, Zeiss, Oberkochen, Germany).

Immunofluorescence image acquisition and analysis

The brain slices labeled for immunofluorescence were acquired using a Leica Stellaris 8 laser-scanning confocal microscope (Leica Microsystems. Biomarker Kft. Budapest, Hungary) with 499-, 554-, and 649-nm lasers for excitation of the fluorophores. The utilized emission filters for these lasers were 504–553, 559–654, and 654–750 nm, respectively. Z-stack images were taken using a HC PL APO CS2 63×/1.40 oil immersion objective in a unidirectional scanning mode. To analyze AIS immunofluorescence in z-stack images, we used an in-house macro of ImageJ software (US National Institutes of Health, Bethesda, MD, USA) and a custom-made script (*86*) developed by Dr. Adam Tiszlavicz to determine the length and proximal and terminal points of the AIS using the Euclidean distance formula by manually

marking the points. We measured the fluorescence intensity profiles along the axon following a polyline of the connected points to establish the entire fluorescence signal line for the immunofluorophore signals. The AIS lengths were normalized (expressed as 10 bins) to the proximal and terminal distances because of the different lengths of the AIS, and the intensity was normalized to the maximum and minimum values of the binned data.

Nucleus collection for patch-sequencing

We collected the nuclei of cells that exhibited the fast-spiking phenotype. Before collecting the data, we made sure to thoroughly clean all surfaces, equipment, and materials by wiping them with DNA AWAY™ (Thermo Fisher Scientific) and RNaseZap™ (Sigma-Aldrich, St. Louis, MO, USA). We cleaned the perfusion with 50 mL of 70% ethanol. After the electrophysiological recording, we centered the pipette on the soma and applied a constant small negative pressure to start extracting the cytosol. This helped attract the nucleus to the tip of the pipette. We maintained the negative pressure and slowly retracted the pipette while monitoring the pipette seal. Once the nucleus was visible on the pipette tip, we increased the speed to remove the pipette from the slice. We then removed the pipette containing the internal solution, cytosol, and nucleus from the pipette holder and expelled its contents into a 0.2-mL tight-lock PCR tube (TubeOne, StarLab, Hamburg, Germany). The tube contained 2 μL of lysis buffer consisting of 0.8% Triton X-100 (Sigma-Aldrich) and 1 U/μL RNase inhibitor (Takara, Kyoto, Japan). The internal solution comprised the following components: 110 mM K-gluconate (Sigma-Aldrich), 4 mM KCl solution, RNase-free (Invitrogen), 10 mM HEPES solution (Sigma-Aldrich), 1 mM ATP-Mg (Sigma-Aldrich), 0.3 mM GTP-Na (Sigma-Aldrich), 10 mM sodium phosphocreatine (Sigma-Aldrich), 0.2 mM EGTA (Sigma-Aldrich), 20 μg/mL RNA-grade glycogen solution (Thermo Fisher Scientific), and 0.5 U/μL RNase inhibitor (Takara). We then spun down the resultant sample (approximately 4.0 μL) for 2 s and placed it on dry ice. Finally, we stored the sample at −80°C until in-tube reverse transcription.

cDNA amplification and library construction

To prepare the libraries, we used a protocol based on the smartseq2 procedure (*87, 88*). Briefly, cDNA was generated and amplified by 24 PCR cycles for all samples, including the negative controls. We augmented the cDNA to add indexes and adapter sequences, pooled them equimolarly, and then sequenced our samples on the Illumina MiSeq platform (Illumina, San Diego, CA, USA) with a 50 single-end read mode. Each sample was sequenced to around 1–2 million reads.

Sequencing data processing

The study used 66-bases paired-end reads that were aligned to GRCh38 using the annotation GTF file (GRCh38_r93) retrieved from Ensembl. Sequence alignment was performed using STAR v2.7.11a (*89*). The default parameters were used with the following arguments: --soloType SmartSeq --soloUMIdedup Exact --soloStrand Unstranded --soloFeatures GeneFull. Full gene counts, including intron and exon counts, produced by STAR were used to calculate the TPM values, which were used for subsequent analyses.

Identification of pvalb neurons based on single-nucleus transcriptomics analysis

The transcriptomic data of individual cells were uploaded to the Allen Institute neuron type identification system to categorize neocortex neuron types by the genes expressed (Allen Institute for Brain Science, 2024, MapMyCells, available from

https://knowledge.brain-map.org/mapmycells/process/ (RRID:SCR_024672)), allowing pvalb neuron identification in cells in which *PVALB/pvalb* expression was below the detection limit. This algorithm uses a set of marker genes to predict the cluster/supertype of the cells based on their corresponding single-nucleus dataset (Fig. S1).

For human samples, the Seattle Alzheimer's Disease Brain Cell Atlas reference taxonomy was used with the Deep Generative Mapping algorithm, whereas mouse cells were classified using the 10X Whole Mouse Brain reference taxonomy with the hierarchical mapping algorithm. Only cells classified as pvalb neurons at $p > 0.9$ were included in further analysis (supertype_bootstrapping_probability). Our single-nucleus gene expression data from human samples highly correlated with the Allen Institute high-resolution database of specific pvalb neuron subtypes (subclass correlation coefficient > 0.5 with the 10X Whole Human Brain dataset using the correlation mapping algorithm) (Fig.7, Fig. S1).

Single-cell model

The three-compartmental model neuron, including its cylindrical dendritic and axonal compartments, was based on the previously described formalism (*28*). The model consisted of a somatic compartment, axonal compartment, and dendritic cable compartment. The axon was 140 µm in length long and 0.8 µm in diameter, and the dendrite was 200 µm in length and 1 µm in diameter. The cable parameters were as follows: axon Ra = from 0.8 to 1.1 MΩ·µm and axon Cm = 6 fF/µm^2. Cm was 2-fold higher for the dendrite (12 fF/µm^2) than for the axon. The ohmic resistance of the somatic compartment was 700 MΩ, and Cm of the somatic compartment was 25 pF. The leakage reversal potential was set to −68 mV. Parameters such as the rheobase and voltage sag were chosen to replicate the basic response properties and were carefully adjusted using the experimental data to attain the best match between the simulated and recorded voltage traces. All intrinsic voltage-dependent currents were calculated using the following equation:

$$I_i = g_i m_i^p h_i (E_i - V),$$

where i represents the individual current type, g_i is the maximal conductance of the current, m_i is the activation variable, p is the exponent of the activation term, h_i is the inactivation variable (either first-order or absent), and E_i is the reversal potential. The activation (m) and inactivation (h) kinetics were modeled according to the following equation:

$$\frac{dx}{dt} = \frac{x_\infty(V) - x}{\tau_x(V)},$$

where x represents m or h, and the voltage-dependent steady-state activation and inactivation are described by the sigmoid function

$$x_\infty(V) = \frac{1}{2} + \frac{1}{2}\tanh\left(\frac{V - V_{x,1/2}}{V_{x,sl}}\right).$$

The midpoint $V_{x,1/2}$ and slope $V_{x,sl}$ parameters of the sigmoids and the other kinetic parameters are presented in (*63*). The tau values (τ) of activation and inactivation were modeled as bell-shaped functions of the Vm (V) according to the following equation:

$$\tau_x(V) = \left(\tau_{x,max} - \tau_{x,min}\right)\left[1 - \tanh\left(\frac{V - V_{\tau x,1/2}}{V_{\tau x,sl}}\right)^2\right] + \tau_{x,min}.$$

The EPSP waveforms were produced by EPSCs with time to peak of 0.5 ms, a decay time constant of 3 ms, reversal potential of 0 mV, and peak conductance range from 6 to 11 nS.

Statistical analysis

The results were systematically presented as the median and IQR. When the parametric distribution was confirmed by the Shapiro–Wilk test ($p \geq 0.05$), statistical significance was tested using Student's t-test or one-way ANOVA with the Bonferroni *post hoc* pairwise test. When significance was indicated by the Shapiro–Wilk test at $p < 0.05$, statistical significance was evaluated using the Mann–Whitney U test, or ANOVA on ranks (Kruskal–Wallis H test) with Dunn's post hoc pairwise test, or one-way MANOVA with the *post hoc* Bonferroni to test differences between multiple samples. For categorical (expressed vs. not expressed) test chi-squared test was used with Benjamini–Hochberg adjustment at the 5% significance level. Correlations were tested using the Spearman Rank order method. Tests were performed using SigmaPlot 15.

References

1. A. A. Galakhova, S. Hunt, R. Wilbers, D. B. Heyer, C. P. J. de Kock, H. D. Mansvelder, N. A. Goriounova, Evolution of cortical neurons supporting human cognition. *Trends Cogn Sci* **26**, 909-922 (2022).
2. R. Nehme, O. Pietilainen, L. E. Barrett, Genomic, molecular, and cellular divergence of the human brain. *Trends Neurosci*, (2024).
3. H. Warming, C. M. Pegasiou, A. P. Pitera, H. Kariis, S. D. Houghton, K. Kurbatskaya, A. Ahmed, P. Grundy, G. Vajramani, D. Bulters, X. Altafaj, K. Deinhardt, M. Vargas-Caballero, A primate-specific short GluN2A-NMDA receptor isoform is expressed in the human brain. *Mol Brain* **12**, 64 (2019).
4. S. Herculano-Houzel, K. Catania, P. R. Manger, J. H. Kaas, Mammalian Brains Are Made of These: A Dataset of the Numbers and Densities of Neuronal and Nonneuronal Cells in the Brain of Glires, Primates, Scandentia, Eulipotyphlans, Afrotherians and Artiodactyls, and Their Relationship with Body Mass. *Brain Behav Evol* **86**, 145-163 (2015).
5. J. Berg, S. A. Sorensen, J. T. Ting, J. A. Miller, T. Chartrand, A. Buchin, T. E. Bakken, A. Budzillo, N. Dee, S. L. Ding, N. W. Gouwens, R. D. Hodge, B.

Kalmbach, C. Lee, B. R. Lee, L. Alfiler, K. Baker, E. Barkan, A. Beller, K. Berry, D. Bertagnolli, K. Bickley, J. Bomben, T. Braun, K. Brouner, T. Casper, P. Chong, K. Crichton, R. Dalley, R. de Frates, T. Desta, S. D. Lee, F. D'Orazi, N. Dotson, T. Egdorf, R. Enstrom, C. Farrell, D. Feng, O. Fong, S. Furdan, A. A. Galakhova, C. Gamlin, A. Gary, A. Glandon, J. Goldy, M. Gorham, N. A. Goriounova, S. Gratiy, L. Graybuck, H. Gu, K. Hadley, N. Hansen, T. S. Heistek, A. M. Henry, D. B. Heyer, D. Hill, C. Hill, M. Hupp, T. Jarsky, S. Kebede, L. Keene, L. Kim, M. H. Kim, M. Kroll, C. Latimer, B. P. Levi, K. E. Link, M. Mallory, R. Mann, D. Marshall, M. Maxwell, M. McGraw, D. McMillen, E. Melief, E. J. Mertens, L. Mezei, N. Mihut, S. Mok, G. Molnar, A. Mukora, L. Ng, K. Ngo, P. R. Nicovich, J. Nyhus, G. Olah, A. Oldre, V. Omstead, A. Ozsvar, D. Park, H. Peng, T. Pham, C. A. Pom, L. Potekhina, R. Rajanbabu, S. Ransford, D. Reid, C. Rimorin, A. Ruiz, D. Sandman, J. Sulc, S. M. Sunkin, A. Szafer, V. Szemenyei, E. R. Thomsen, M. Tieu, A. Torkelson, J. Trinh, H. Tung, W. Wakeman, F. Waleboer, K. Ward, R. Wilbers, G. Williams, Z. Yao, J. G. Yoon, C. Anastassiou, A. Arkhipov, P. Barzo, A. Bernard, C. Cobbs, P. C. de Witt Hamer, R. G. Ellenbogen, L. Esposito, M. Ferreira, R. P. Gwinn, M. J. Hawrylycz, P. R. Hof, S. Idema, A. R. Jones, C. D. Keene, A. L. Ko, G. J. Murphy, L. Ng, J. G. Ojemann, A. P. Patel, J. W. Phillips, D. L. Silbergeld, K. Smith, B. Tasic, R. Yuste, I. Segev, C. P. J. de Kock, H. D. Mansvelder, G. Tamas, H. Zeng, C. Koch, E. S. Lein, Human neocortical expansion involves glutamatergic neuron diversification. *Nature* **598**, 151-158 (2021).

6. R. D. Hodge, T. E. Bakken, J. A. Miller, K. A. Smith, E. R. Barkan, L. T. Graybuck, J. L. Close, B. Long, N. Johansen, O. Penn, Z. Yao, J. Eggermont, T. Hollt, B. P. Levi, S. I. Shehata, B. Aevermann, A. Beller, D. Bertagnolli, K. Brouner, T. Casper, C. Cobbs, R. Dalley, N. Dee, S. L. Ding, R. G. Ellenbogen, O. Fong, E. Garren, J. Goldy, R. P. Gwinn, D. Hirschstein, C. D. Keene, M. Keshk, A. L. Ko, K. Lathia, A. Mahfouz, Z. Maltzer, M. McGraw, T. N. Nguyen, J. Nyhus, J. G. Ojemann, A. Oldre, S. Parry, S. Reynolds, C. Rimorin, N. V. Shapovalova, S. Somasundaram, A. Szafer, E. R. Thomsen, M. Tieu, G. Quon, R. H. Scheuermann, R. Yuste, S. M. Sunkin, B. Lelieveldt, D. Feng, L. Ng, A. Bernard, M. Hawrylycz, J. W. Phillips, B. Tasic, H. Zeng, A. R. Jones, C. Koch, E. S. Lein, Conserved cell types with divergent features in human versus mouse cortex. *Nature* **573**, 61-68 (2019).
7. H. Zeng, E. H. Shen, J. G. Hohmann, S. W. Oh, A. Bernard, J. J. Royall, K. J. Glattfelder, S. M. Sunkin, J. A. Morris, A. L. Guillozet-Bongaarts, K. A. Smith, A. J. Ebbert, B. Swanson, L. Kuan, D. T. Page, C. C. Overly, E. S. Lein, M. J. Hawrylycz, P. R. Hof, T. M. Hyde, J. E. Kleinman, A. R. Jones, Large-scale cellular-resolution gene profiling in human neocortex reveals species-specific molecular signatures. *Cell* **149**, 483-496 (2012).
8. H. Suresh, M. Crow, N. Jorstad, R. Hodge, E. Lein, A. Dobin, T. Bakken, J. Gillis, Comparative single-cell transcriptomic analysis of primate brains highlights human-specific regulatory evolution. *Nat Ecol Evol* **7**, 1930-1943 (2023).
9. F. Rossi, Evolutionary Mechanisms and Neural Adaptation: Selective Versus Constructive Strategies in the Development and Plasticity of the Nervous System. . *In: Fasolo, A. (eds) The Theory of Evolution and Its Impact. Springer, Milano.*, (2012).
10. A. Beauchamp, Y. Yee, B. C. Darwin, A. Raznahan, R. B. Mars, J. P. Lerch, Whole-brain comparison of rodent and human brains using spatial transcriptomics. *Elife* **11**, (2022).
11. E. Boldog, T. E. Bakken, R. D. Hodge, M. Novotny, B. D. Aevermann, J. Baka, S. Borde, J. L. Close, F. Diez-Fuertes, S. L. Ding, N. Farago, A. K. Kocsis, B. Kovacs,

Z. Maltzer, J. M. McCorrison, J. A. Miller, G. Molnar, G. Olah, A. Ozsvar, M. Rozsa, S. I. Shehata, K. A. Smith, S. M. Sunkin, D. N. Tran, P. Venepally, A. Wall, L. G. Puskas, P. Barzo, F. J. Steemers, N. J. Schork, R. H. Scheuermann, R. S. Lasken, E. S. Lein, G. Tamas, Transcriptomic and morphophysiological evidence for a specialized human cortical GABAergic cell type. *Nat Neurosci* **21**, 1185-1195 (2018).

12. L. Campagnola, S. C. Seeman, T. Chartrand, L. Kim, A. Hoggarth, C. Gamlin, S. Ito, J. Trinh, P. Davoudian, C. Radaelli, M. H. Kim, T. Hage, T. Braun, L. Alfiler, J. Andrade, P. Bohn, R. Dalley, A. Henry, S. Kebede, M. Alice, D. Sandman, G. Williams, R. Larsen, C. Teeter, T. L. Daigle, K. Berry, N. Dotson, R. Enstrom, M. Gorham, M. Hupp, S. Dingman Lee, K. Ngo, P. R. Nicovich, L. Potekhina, S. Ransford, A. Gary, J. Goldy, D. McMillen, T. Pham, M. Tieu, L. Siverts, M. Walker, C. Farrell, M. Schroedter, C. Slaughterbeck, C. Cobb, R. Ellenbogen, R. P. Gwinn, C. D. Keene, A. L. Ko, J. G. Ojemann, D. L. Silbergeld, D. Carey, T. Casper, K. Crichton, M. Clark, N. Dee, L. Ellingwood, J. Gloe, M. Kroll, J. Sulc, H. Tung, K. Wadhwani, K. Brouner, T. Egdorf, M. Maxwell, M. McGraw, C. A. Pom, A. Ruiz, J. Bomben, D. Feng, N. Hejazinia, S. Shi, A. Szafer, W. Wakeman, J. Phillips, A. Bernard, L. Esposito, F. D. D'Orazi, S. Sunkin, K. Smith, B. Tasic, A. Arkhipov, S. Sorensen, E. Lein, C. Koch, G. Murphy, H. Zeng, T. Jarsky, Local connectivity and synaptic dynamics in mouse and human neocortex. *Science* **375**, eabj5861 (2022).

13. R. Chittajallu, K. Auville, V. Mahadevan, M. Lai, S. Hunt, D. Calvigioni, K. A. Pelkey, K. A. Zaghloul, C. J. McBain, Activity-dependent tuning of intrinsic excitability in mouse and human neurogliaform cells. *Elife* **9**, (2020).

14. G. J. Clowry, An enhanced role and expanded developmental origins for gamma-aminobutyric acidergic interneurons in the human cerebral cortex. *J Anat* **227**, 384-393 (2015).

15. C. Dehay, W. B. Huttner, Development and evolution of the primate neocortex from a progenitor cell perspective. *Development* **151**, (2024).

16. D. B. Heyer, R. Wilbers, A. A. Galakhova, E. Hartsema, S. Braak, S. Hunt, M. B. Verhoog, M. L. Muijtjens, E. J. Mertens, S. Idema, J. C. Baayen, P. de Witt Hamer, M. Klein, M. McGraw, E. S. Lein, C. P. J. de Kock, H. D. Mansvelder, N. A. Goriounova, Verbal and General IQ Associate with Supragranular Layer Thickness and Cell Properties of the Left Temporal Cortex. *Cereb Cortex* **32**, 2343-2357 (2022).

17. X. Hu, B. R. Rocco, C. Fee, E. Sibille, Cell Type-Specific Gene Expression of Alpha 5 Subunit-Containing Gamma-Aminobutyric Acid Subtype A Receptors in Human and Mouse Frontal Cortex. *Mol Neuropsychiatry* **4**, 204-215 (2019).

18. N. L. Jorstad, J. H. T. Song, D. Exposito-Alonso, H. Suresh, N. Castro-Pacheco, F. M. Krienen, A. M. Yanny, J. Close, E. Gelfand, B. Long, S. C. Seeman, K. J. Travaglini, S. Basu, M. Beaudin, D. Bertagnolli, M. Crow, S. L. Ding, J. Eggermont, A. Glandon, J. Goldy, K. Kiick, T. Kroes, D. McMillen, T. Pham, C. Rimorin, K. Siletti, S. Somasundaram, M. Tieu, A. Torkelson, G. Feng, W. D. Hopkins, T. Hollt, C. D. Keene, S. Linnarsson, S. A. McCarroll, B. P. Lelieveldt, C. C. Sherwood, K. Smith, C. A. Walsh, A. Dobin, J. Gillis, E. S. Lein, R. D. Hodge, T. E. Bakken, Comparative transcriptomics reveals human-specific cortical features. *Science* **382**, eade9516 (2023).

19. B. E. Kalmbach, A. Buchin, B. Long, J. Close, A. Nandi, J. A. Miller, T. E. Bakken, R. D. Hodge, P. Chong, R. de Frates, K. Dai, Z. Maltzer, P. R. Nicovich, C. D. Keene, D. L. Silbergeld, R. P. Gwinn, C. Cobbs, A. L. Ko, J. G. Ojemann, C. Koch, C. A. Anastassiou, E. S. Lein, J. T. Ting, h-Channels Contribute to Divergent Intrinsic Membrane Properties of Supragranular Pyramidal Neurons in Human versus Mouse Cerebral Cortex. *Neuron* **100**, 1194-1208 e1195 (2018).

20. G. M. Shepherd, T. B. Rowe, Neocortical Lamination: Insights from Neuron Types and Evolutionary Precursors. *Front Neuroanat* **11**, 100 (2017).
21. L. Lim, D. Mi, A. Llorca, O. Marin, Development and Functional Diversification of Cortical Interneurons. *Neuron* **100**, 294-313 (2018).
22. R. Tremblay, S. Lee, B. Rudy, GABAergic Interneurons in the Neocortex: From Cellular Properties to Circuits. *Neuron* **91**, 260-292 (2016).
23. B. R. Lee, R. Dalley, J. A. Miller, T. Chartrand, J. Close, R. Mann, A. Mukora, L. Ng, L. Alfiler, K. Baker, D. Bertagnolli, K. Brouner, T. Casper, E. Csajbok, N. Donadio, S. L. W. Driessens, T. Egdorf, R. Enstrom, A. A. Galakhova, A. Gary, E. Gelfand, J. Goldy, K. Hadley, T. S. Heistek, D. Hill, W. H. Hou, N. Johansen, N. Jorstad, L. Kim, A. K. Kocsis, L. Kruse, M. Kunst, G. Leon, B. Long, M. Mallory, M. Maxwell, M. McGraw, D. McMillen, E. J. Melief, G. Molnar, M. T. Mortrud, D. Newman, J. Nyhus, X. Opitz-Araya, A. Ozsvar, T. Pham, A. Pom, L. Potekhina, R. Rajanbabu, A. Ruiz, S. M. Sunkin, I. Szots, N. Taskin, B. Thyagarajan, M. Tieu, J. Trinh, S. Vargas, D. Vumbaco, F. Waleboer, S. Walling-Bell, N. Weed, G. Williams, J. Wilson, S. Yao, T. Zhou, P. Barzo, T. Bakken, C. Cobbs, N. Dee, R. G. Ellenbogen, L. Esposito, M. Ferreira, N. W. Gouwens, B. Grannan, R. P. Gwinn, J. S. Hauptman, R. Hodge, T. Jarsky, C. D. Keene, A. L. Ko, A. R. Korshoej, B. P. Levi, K. Meier, J. G. Ojemann, A. Patel, J. Ruzevick, D. L. Silbergeld, K. Smith, J. C. Sorensen, J. Waters, H. Zeng, J. Berg, M. Capogna, N. A. Goriounova, B. Kalmbach, C. P. J. de Kock, H. D. Mansvelder, S. A. Sorensen, G. Tamas, E. S. Lein, J. T. Ting, Signature morphoelectric properties of diverse GABAergic interneurons in the human neocortex. *Science* **382**, eadf6484 (2023).
24. B. Mihaljevic, P. Larranaga, C. Bielza, Comparing the Electrophysiology and Morphology of Human and Mouse Layer 2/3 Pyramidal Neurons With Bayesian Networks. *Front Neuroinform* **15**, 580873 (2021).
25. H. Moradi Chameh, S. Rich, L. Wang, F. D. Chen, L. Zhang, P. L. Carlen, S. J. Tripathy, T. A. Valiante, Diversity amongst human cortical pyramidal neurons revealed via their sag currents and frequency preferences. *Nat Commun* **12**, 2497 (2021).
26. S. Olah, G. Komlosi, J. Szabadics, C. Varga, E. Toth, P. Barzo, G. Tamas, Output of neurogliaform cells to various neuron types in the human and rat cerebral cortex. *Front Neural Circuits* **1**, 4 (2007).
27. R. B. Poorthuis, K. Muhammad, M. Wang, M. B. Verhoog, S. Junek, A. Wrana, H. D. Mansvelder, J. J. Letzkus, Rapid Neuromodulation of Layer 1 Interneurons in Human Neocortex. *Cell Rep* **23**, 951-958 (2018).
28. V. Szegedi, E. Bakos, S. Furdan, B. H. Kovacs, D. Varga, M. Erdelyi, P. Barzo, A. Szucs, G. Tamas, K. Lamsa, HCN channels at the cell soma ensure the rapid electrical reactivity of fast-spiking interneurons in human neocortex. *PLoS Biol* **21**, e3002001 (2023).
29. G. Testa-Silva, M. Rosier, S. Honnuraiah, R. Guzulaitis, A. M. Megias, C. French, J. King, K. Drummond, L. M. Palmer, G. J. Stuart, High synaptic threshold for dendritic NMDA spike generation in human layer 2/3 pyramidal neurons. *Cell Rep* **41**, 111787 (2022).
30. M. B. Verhoog, N. A. Goriounova, J. Obermayer, J. Stroeder, J. J. Hjorth, G. Testa-Silva, J. C. Baayen, C. P. de Kock, R. M. Meredith, H. D. Mansvelder, Mechanisms underlying the rules for associative plasticity at adult human neocortical synapses. *J Neurosci* **33**, 17197-17208 (2013).
31. R. Wilbers, A. A. Galakhova, S. L. W. Driessens, T. S. Heistek, V. D. Metodieva, J. Hagemann, D. B. Heyer, E. J. Mertens, S. Deng, S. Idema, P. C. de Witt Hamer, D. P.

Noske, P. van Schie, I. Kommers, G. Luan, T. Li, Y. Shu, C. P. J. de Kock, H. D. Mansvelder, N. A. Goriounova, Structural and functional specializations of human fast-spiking neurons support fast cortical signaling. *Sci Adv* **9**, eadf0708 (2023).

32. L. Krubitzer, In search of a unifying theory of complex brain evolution. *Ann N Y Acad Sci* **1156**, 44-67 (2009).
33. S. Rich, H. Moradi Chameh, V. Sekulic, T. A. Valiante, F. K. Skinner, Modeling Reveals Human-Rodent Differences in H-Current Kinetics Influencing Resonance in Cortical Layer 5 Neurons. *Cereb Cortex* **31**, 845-872 (2021).
34. B. Libe-Philippot, A. Lejeune, K. Wierda, N. Louros, E. Erkol, I. Vlaeminck, S. Beckers, V. Gaspariunaite, A. Bilheu, K. Konstantoulea, H. Nyitrai, M. De Vleeschouwer, K. M. Vennekens, N. Vidal, T. W. Bird, D. C. Soto, T. Jaspers, M. Dewilde, M. Y. Dennis, F. Rousseau, D. Comoletti, J. Schymkowitz, T. Theys, J. de Wit, P. Vanderhaeghen, LRRC37B is a human modifier of voltage-gated sodium channels and axon excitability in cortical neurons. *Cell* **186**, 5766-5783 e5725 (2023).
35. E. J. Mertens, Y. Leibner, J. Pie, A. A. Galakhova, F. Waleboer, J. Meijer, T. S. Heistek, R. Wilbers, D. Heyer, N. A. Goriounova, S. Idema, M. B. Verhoog, B. E. Kalmbach, B. R. Lee, R. P. Gwinn, E. S. Lein, E. Aronica, J. Ting, H. D. Mansvelder, I. Segev, C. P. J. de Kock, Morpho-electric diversity of human hippocampal CA1 pyramidal neurons. *Cell Rep* **43**, 114100 (2024).
36. N. V. Povysheva, A. V. Zaitsev, D. C. Rotaru, G. Gonzalez-Burgos, D. A. Lewis, L. S. Krimer, Parvalbumin-positive basket interneurons in monkey and rat prefrontal cortex. *J Neurophysiol* **100**, 2348-2360 (2008).
37. B. Wang, W. Ke, J. Guang, G. Chen, L. Yin, S. Deng, Q. He, Y. Liu, T. He, R. Zheng, Y. Jiang, X. Zhang, T. Li, G. Luan, H. D. Lu, M. Zhang, X. Zhang, Y. Shu, Firing Frequency Maxima of Fast-Spiking Neurons in Human, Monkey, and Mouse Neocortex. *Front Cell Neurosci* **10**, 239 (2016).
38. V. Szegedi, G. Molnar, M. Paizs, E. Csakvari, P. Barzo, G. Tamas, K. Lamsa, High-Precision Fast-Spiking Basket Cell Discharges during Complex Events in the Human Neocortex. *eNeuro* **4**, (2017).
39. V. Szegedi, M. Paizs, J. Baka, P. Barzo, G. Molnar, G. Tamas, K. Lamsa, Robust perisomatic GABAergic self-innervation inhibits basket cells in the human and mouse supragranular neocortex. *Elife* **9**, (2020).
40. S. Hijazi, A. B. Smit, R. E. van Kesteren, Fast-spiking parvalbumin-positive interneurons in brain physiology and Alzheimer's disease. *Mol Psychiatry*, (2023).
41. C. Y. Huang, M. N. Rasband, Axon initial segments: structure, function, and disease. *Ann N Y Acad Sci* **1420**, 46-61 (2018).
42. C. Leterrier, The Axon Initial Segment: An Updated Viewpoint. *J Neurosci* **38**, 2135-2145 (2018).
43. H. Hu, J. Gan, P. Jonas, Interneurons. Fast-spiking, parvalbumin(+) GABAergic interneurons: from cellular design to microcircuit function. *Science* **345**, 1255263 (2014).
44. T. Li, C. Tian, P. Scalmani, C. Frassoni, M. Mantegazza, Y. Wang, M. Yang, S. Wu, Y. Shu, Action potential initiation in neocortical inhibitory interneurons. *PLoS Biol* **12**, e1001944 (2014).
45. R. Yamada, H. Kuba, Structural and Functional Plasticity at the Axon Initial Segment. *Front Cell Neurosci* **10**, 250 (2016).
46. Y. Yang, Y. Ogawa, K. L. Hedstrom, M. N. Rasband, betaIV spectrin is recruited to axon initial segments and nodes of Ranvier by ankyrinG. *J Cell Biol* **176**, 509-519 (2007).

47. S. L. Jones, T. M. Svitkina, Axon Initial Segment Cytoskeleton: Architecture, Development, and Role in Neuron Polarity. *Neural Plast* **2016**, 6808293 (2016).
48. S. Goethals, R. Brette, Theoretical relation between axon initial segment geometry and excitability. *Elife* **9**, (2020).
49. M. H. Kole, G. J. Stuart, Signal processing in the axon initial segment. *Neuron* **73**, 235-247 (2012).
50. H. Kuba, H. Ohmori, Roles of axonal sodium channels in precise auditory time coding at nucleus magnocellularis of the chick. *J Physiol* **587**, 87-100 (2009).
51. A. Lorincz, Z. Nusser, Cell-type-dependent molecular composition of the axon initial segment. *J Neurosci* **28**, 14329-14340 (2008).
52. J. E. O'Brien, M. H. Meisler, Sodium channel SCN8A (Nav1.6): properties and de novo mutations in epileptic encephalopathy and intellectual disability. *Front Genet* **4**, 213 (2013).
53. E. M. Goldberg, B. D. Clark, E. Zagha, M. Nahmani, A. Erisir, B. Rudy, K+ channels at the axon initial segment dampen near-threshold excitability of neocortical fast-spiking GABAergic interneurons. *Neuron* **58**, 387-400 (2008).
54. M. H. Kole, J. J. Letzkus, G. J. Stuart, Axon initial segment Kv1 channels control axonal action potential waveform and synaptic efficacy. *Neuron* **55**, 633-647 (2007).
55. C. Gu, J. Barry, Function and mechanism of axonal targeting of voltage-sensitive potassium channels. *Prog Neurobiol* **94**, 115-132 (2011).
56. M. C. D'Adamo, A. Liantonio, J. F. Rolland, M. Pessia, P. Imbrici, Kv1.1 Channelopathies: Pathophysiological Mechanisms and Therapeutic Approaches. *Int J Mol Sci* **21**, (2020).
57. Y. Ogawa, I. Horresh, J. S. Trimmer, D. S. Bredt, E. Peles, M. N. Rasband, Postsynaptic density-93 clusters Kv1 channels at axon initial segments independently of Caspr2. *J Neurosci* **28**, 5731-5739 (2008).
58. M. H. Higgs, W. J. Spain, Kv1 channels control spike threshold dynamics and spike timing in cortical pyramidal neurones. *J Physiol* **589**, 5125-5142 (2011).
59. M. Shao, W. Zhang, Y. Li, L. Tang, Z. Z. Hao, S. Liu, Patch-seq: Advances and Biological Applications. *Cell Mol Neurobiol* **44**, 8 (2023).
60. C. R. Cadwell, A. S. Tolias, Patch-seq: Multimodal Profiling of Single-Cell Morphology, Electrophysiology, and Gene Expression. *Methods Mol Biol* **2752**, 227-243 (2024).
61. A. Chow, A. Erisir, C. Farb, M. S. Nadal, A. Ozaita, D. Lau, E. Welker, B. Rudy, K(+) channel expression distinguishes subpopulations of parvalbumin- and somatostatin-containing neocortical interneurons. *J Neurosci* **19**, 9332-9345 (1999).
62. M. Martina, J. H. Schultz, H. Ehmke, H. Monyer, P. Jonas, Functional and molecular differences between voltage-gated K+ channels of fast-spiking interneurons and pyramidal neurons of rat hippocampus. *J Neurosci* **18**, 8111-8125 (1998).
63. V. Szegedi, A. Tiszlavicz, S. Furdan, A. Douida, E. Bakos, P. Barzo, G. Tamas, A. Szucs, K. Lamsa, Aging-associated weakening of the action potential in fast-spiking interneurons in the human neocortex. *J Biotechnol* **389**, 1-12 (2024).
64. L. Krubitzer, J. Kaas, The evolution of the neocortex in mammals: how is phenotypic diversity generated? *Curr Opin Neurobiol* **15**, 444-453 (2005).
65. R. Blekhman, A. Oshlack, A. E. Chabot, G. K. Smyth, Y. Gilad, Gene regulation in primates evolves under tissue-specific selection pressures. *PLoS Genet* **4**, e1000271 (2008).
66. E. J. Vallender, N. Mekel-Bobrov, B. T. Lahn, Genetic basis of human brain evolution. *Trends Neurosci* **31**, 637-644 (2008).

67. M. A. Rosales-Reynoso, C. I. Juarez-Vazquez, P. Barros-Nunez, Evolution and genomics of the human brain. *Neurologia (Engl Ed)* **33**, 254-265 (2018).
68. E. Caglayan, F. Ayhan, Y. Liu, R. M. Vollmer, E. Oh, C. C. Sherwood, T. M. Preuss, S. V. Yi, G. Konopka, Molecular features driving cellular complexity of human brain evolution. *Nature* **620**, 145-153 (2023).
69. Y. Zhou, H. Song, G. L. Ming, Genetics of human brain development. *Nat Rev Genet* **25**, 26-45 (2024).
70. Y. Kawaguchi, Y. Kubota, GABAergic cell subtypes and their synaptic connections in rat frontal cortex. *Cereb Cortex* **7**, 476-486 (1997).
71. Y. Gonchar, Q. Wang, A. Burkhalter, Multiple distinct subtypes of GABAergic neurons in mouse visual cortex identified by triple immunostaining. *Front Neuroanat* **1**, 3 (2007).
72. J. B. Ruden, L. L. Dugan, C. Konradi, Parvalbumin interneuron vulnerability and brain disorders. *Neuropsychopharmacology* **46**, 279-287 (2021).
73. D. A. Lewis, A. A. Curley, J. R. Glausier, D. W. Volk, Cortical parvalbumin interneurons and cognitive dysfunction in schizophrenia. *Trends Neurosci* **35**, 57-67 (2012).
74. L. Nahar, B. M. Delacroix, H. W. Nam, The Role of Parvalbumin Interneurons in Neurotransmitter Balance and Neurological Disease. *Front Psychiatry* **12**, 679960 (2021).
75. O. Marin, Parvalbumin interneuron deficits in schizophrenia. *Eur Neuropsychopharmacol* **82**, 44-52 (2024).
76. S. G. Brickley, V. Revilla, S. G. Cull-Candy, W. Wisden, M. Farrant, Adaptive regulation of neuronal excitability by a voltage-independent potassium conductance. *Nature* **409**, 88-92 (2001).
77. C. N. Hall, M. C. Klein-Flugge, C. Howarth, D. Attwell, Oxidative phosphorylation, not glycolysis, powers presynaptic and postsynaptic mechanisms underlying brain information processing. *J Neurosci* **32**, 8940-8951 (2012).
78. C. Howarth, P. Gleeson, D. Attwell, Updated energy budgets for neural computation in the neocortex and cerebellum. *J Cereb Blood Flow Metab* **32**, 1222-1232 (2012).
79. J. S. McCasland, L. S. Hibbard, GABAergic neurons in barrel cortex show strong, whisker-dependent metabolic activation during normal behavior. *J Neurosci* **17**, 5509-5527 (1997).
80. O. Kann, I. E. Papageorgiou, A. Draguhn, Highly energized inhibitory interneurons are a central element for information processing in cortical networks. *J Cereb Blood Flow Metab* **34**, 1270-1282 (2014).
81. E. Ghirardini, G. Sagona, A. Marquez-Galera, F. Calugi, C. M. Navarron, F. Cacciante, S. Chen, F. Di Vetta, L. Dada, R. Mazziotti, L. Lupori, E. Putignano, P. Baldi, J. P. Lopez-Atalaya, T. Pizzorusso, L. Baroncelli, Cell-specific vulnerability to metabolic failure: the crucial role of parvalbumin expressing neurons in creatine transporter deficiency. *Acta Neuropathol Commun* **11**, 34 (2023).
82. K. Fonseca-Azevedo, S. Herculano-Houzel, Metabolic constraint imposes tradeoff between body size and number of brain neurons in human evolution. *Proc Natl Acad Sci U S A* **109**, 18571-18576 (2012).
83. H. Pontzer, M. H. Brown, D. A. Raichlen, H. Dunsworth, B. Hare, K. Walker, A. Luke, L. R. Dugas, R. Durazo-Arvizu, D. Schoeller, J. Plange-Rhule, P. Bovet, T. E. Forrester, E. V. Lambert, M. E. Thompson, R. W. Shumaker, S. R. Ross, Metabolic acceleration and the evolution of human brain size and life history. *Nature* **533**, 390-392 (2016).

84. F. Hofflin, A. Jack, C. Riedel, J. Mack-Bucher, J. Roos, C. Corcelli, C. Schultz, P. Wahle, M. Engelhardt, Heterogeneity of the Axon Initial Segment in Interneurons and Pyramidal Cells of Rodent Visual Cortex. *Front Cell Neurosci* **11**, 332 (2017).
85. M. S. Hamada, S. Goethals, S. I. de Vries, R. Brette, M. H. Kole, Covariation of axon initial segment location and dendritic tree normalizes the somatic action potential. *Proc Natl Acad Sci U S A* **113**, 14841-14846 (2016).
86. J. Ollion, J. Cochennec, F. Loll, C. Escude, T. Boudier, TANGO: a generic tool for high-throughput 3D image analysis for studying nuclear organization. *Bioinformatics* **29**, 1840-1841 (2013).
87. S. Picelli, O. R. Faridani, A. K. Bjorklund, G. Winberg, S. Sagasser, R. Sandberg, Full-length RNA-seq from single cells using Smart-seq2. *Nat Protoc* **9**, 171-181 (2014).
88. B. P. Hennig, L. Velten, I. Racke, C. S. Tu, M. Thoms, V. Rybin, H. Besir, K. Remans, L. M. Steinmetz, Large-Scale Low-Cost NGS Library Preparation Using a Robust Tn5 Purification and Tagmentation Protocol. *G3 (Bethesda)* **8**, 79-89 (2018).
89. A. Dobin, C. A. Davis, F. Schlesinger, J. Drenkow, C. Zaleski, S. Jha, P. Batut, M. Chaisson, T. R. Gingeras, STAR: ultrafast universal RNA-seq aligner. *Bioinformatics* **29**, 15-21 (2013).
90. A. Erisir, D. Lau, B. Rudy, C. S. Leonard, Function of specific K(+) channels in sustained high-frequency firing of fast-spiking neocortical interneurons. *J Neurophysiol* **82**, 2476-2489 (1999).

Acknowledgments: We thank Dr. Ferhan Ayaydin at the Functional Cell Biology and Immunology Advanced Core Facility of Hungarian Center of Excellence for Molecular Medicine and Szeged University and Dr. Fanni Nedenyi at HCEMM for help with the statistical analyses. The funders played no role in the study design, data collection and analysis, decision to publish, or preparation of the manuscript.

Funding: Project no. TKP-2021-EGA-05 was implemented with the support provided by the Ministry of Culture and Innovation of Hungary from the National Research, Development and Innovation Fund, financed under the TKP2021-EGA funding scheme (K.L). Project no. 2022-2.1.1-NL-2022-00005 was implemented with the support provided by the Ministry of Culture and Innovation of Hungary from the National Research, Development and Innovation Fund, financed under the 2022-2.1.1-NL funding scheme (K.L). EU's Horizon 2020 research and innovation program under grant agreement No. 739593 (K.L). Nemzeti Kutatási, Fejlesztési és Innovációs Alap, OTKA K 134279 Magyar Tudományos Akadémia - the National Brain Research Program Hungary (K.L). The Hungarian Scientific Research Foundation grant number ANN-135291 (K.L). Eötvös Loránd Research Network grants ELKH-SZTE Agykérgi Neuronhálózatok Kutatócsoport and KÖ-36/2021 (G.T.). Ministry of Human Capacities Hungary (20391-3/2018/FEKUSTRAT (G.T.) and NKP 16-3-VIII-3) (G.T.). National Research, Development and Innovation Office grants GINOP 2.3.2-15-2016-00018 (G.T). Élvonal KKP 133807 (G.T.), ÚNKP-20-5 - SZTE-681 (G.T.), 2019-2.1.7-ERA-NET-2022-00038 (G.T.), TKP2021-EGA-09 (G.T.), TKP-2021-EGA-28 (G.T.) and OTKA K128863 (G.T.). National Institutes of Health awards U01MH114812 (G.T.) and UM1MH130981 (G.T.). National Research, Development and Innovation Office, grant No. ANN_135291 (AS).

Author contributions: Conceptualization: K.L. and V.S. Methodology: A.S., A.T., P.B, B.B, G.H, G.T, and V.B. Investigation: E.B, A.T, V.S, A.D, D.W, J.L, S.F. and A.S. Data curation: V.S, A.D. and E.B. Formal analysis: A.T., E.B., V.S. and S.F. Supervision: K.L. Project administration: K.L. and V.S. Funding acquisition: K.L., G.T, A.S. Writing original draft: K.L. Writing review and editing: K.L.

Competing interests: The authors declare that they have no competing interests.

Data and materials availability: All data needed to evaluate the conclusions in the paper are present in the paper and/or the Supplementary Materials. All datasets and custom codes used in this study are stored in Hungarian Center of Excellence for Molecular Medicine, Szeged, Hungary, and available on request from the corresponding author.

Figures and Tables

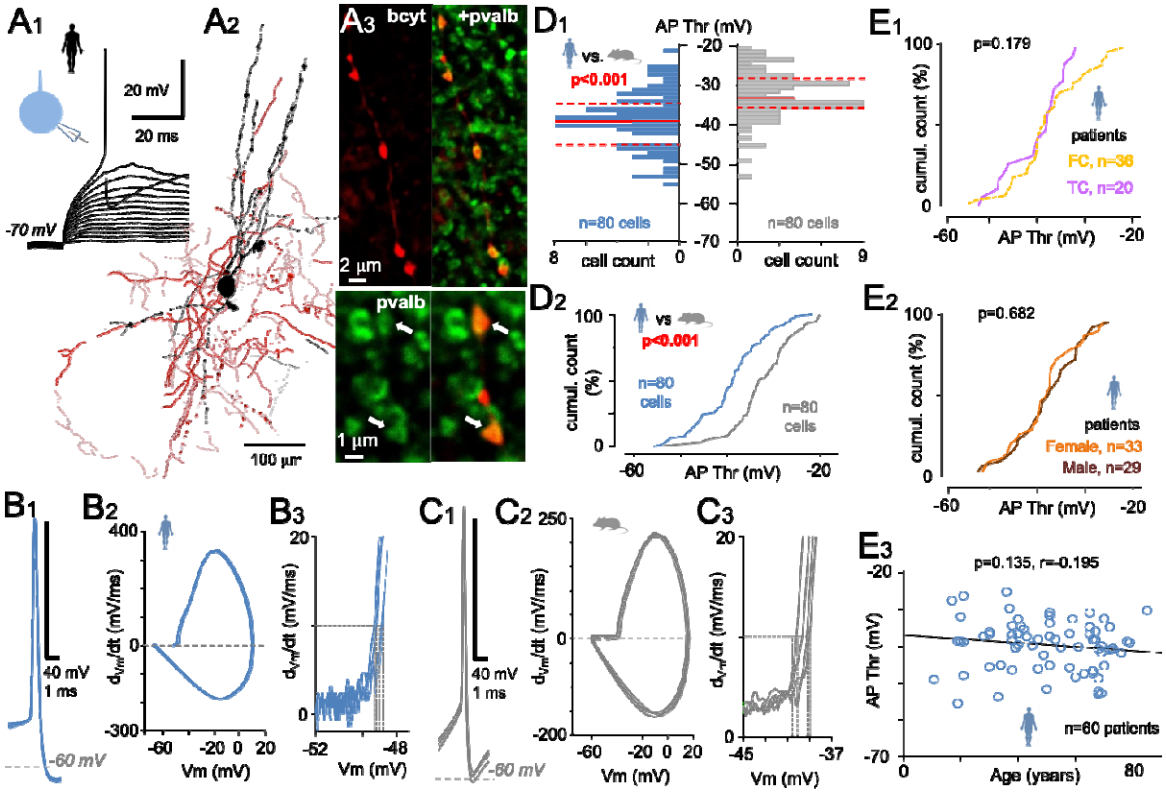

Fig. 1. Lowered AP firing threshold in fast-spiking pvalb interneurons in human compared with mouse neocortex. (A) The AP firing threshold was studied in layer L2/3 interneurons exhibiting a positive immunoreaction for the marker protein pvalb. (A1) Excitatory Vm steps (incremental amplitude steps in whole-cell current clamp in the cell soma at −70 mV) were applied to unveil the AP threshold. (A2) Human neocortex pvalb neurons visualized following whole-cell recording. The soma and dendrites (red) and the axon (black) filled with biocytin and visualized in three merged 50-µm-thick sections are presented. (A3) Confocal microscope images illustrate the positive immunoreaction for pvalb (Alexa 488) in the biocytin-filled axon (bcyt, cy3). Arrows denote the colocalization of the immunoreactions.

(B–C) The AP phase plot defines the firing threshold. (B1) Superimposed APs (four), evoked as presented in *A1*, in human pvalb cells. (B2) Phase plots of the APs exhibiting the first derivative (dV/dt) against Vm (four curves superimposed). (B3) Zoom-in to the AP phase plot curves presenting the initial rise speed of the AP. Dotted vertical lines denote the AP firing threshold, defined as the Vm at which the rise speed reaches 10 mV/ms (horizontal dotted line). (C1) Mouse pvalb cell APs (four superimposed), their phase plots (C2), and the definition of the firing threshold (C3).

(D) Pvalb neurons in humans exhibit a lower AP firing threshold than those in mice (Student's *t*-test). (D1) Histograms of the AP firing threshold in humans (blue, 80 cells) and mice (gray, 80 cells). Bin, 1 mV. The median and quartiles are indicated by solid and dotted red lines, respectively. (D2) The AP firing threshold in human (blue) and mouse (gray) pvalb cells is presented with a cumulative histogram.

(E) The AP firing threshold in human pvalb neurons, presented as the average AP per patient, is not dependent on (E1) the neocortical region (n = 36 patients studied for the frontal cortex [FC]; n = 20 patients for the temporal cortex [TC]). (E2) The AP threshold (average per patient) did not differ between the sexes (33 females, 29 males; Mann–Whitney U-test). (E3) The AP threshold (average per patient) is not associated with patient age (n = 60; Spearman's correlation test). The dotted line denotes the regression.

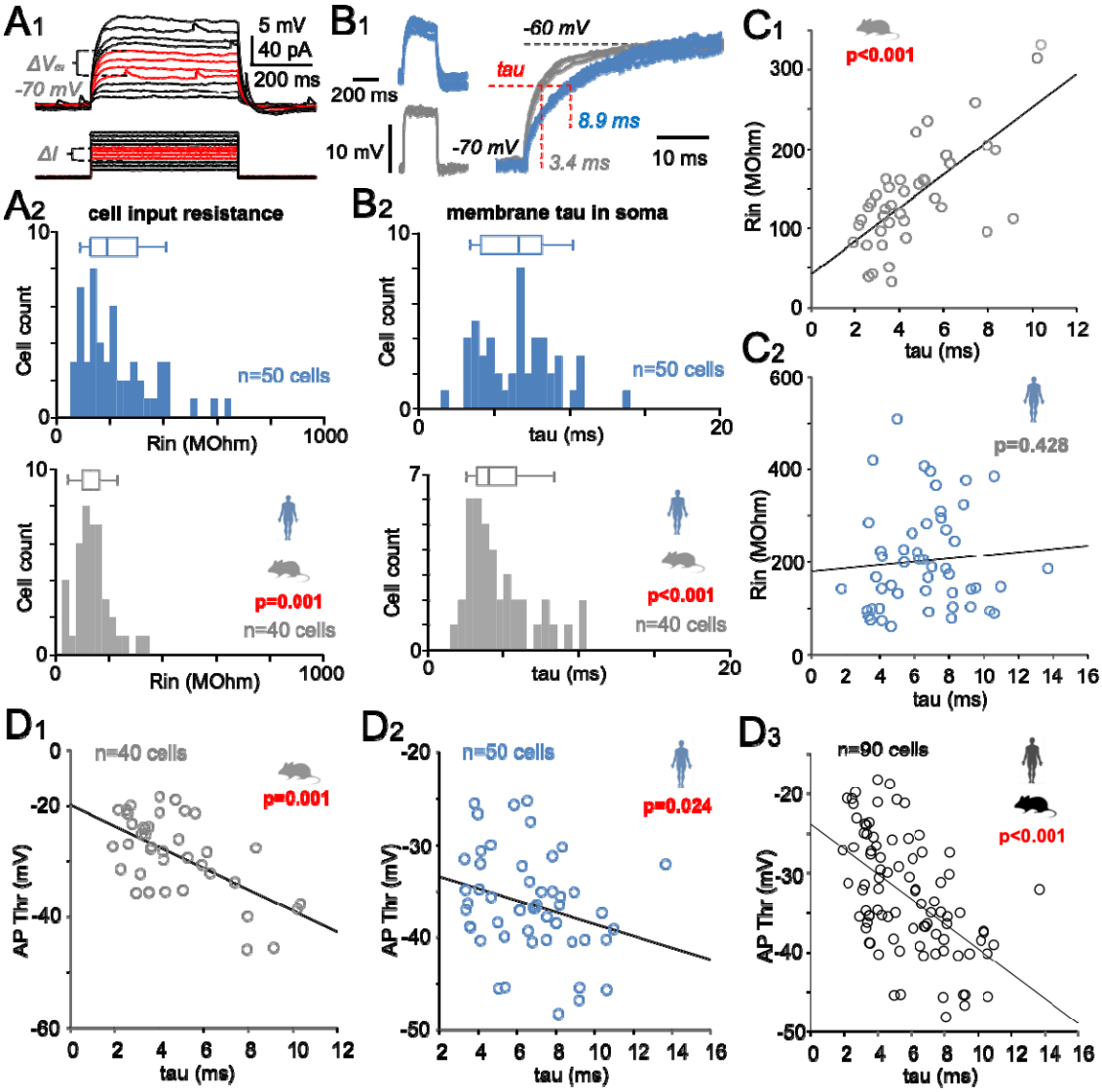

Fig. 2. A low AP firing threshold in pvalb interneurons is associated with an electrically slow soma. (A) Pvalb cells in humans exhibit higher Rin than those in mice at the Vm between −70 mV and the AP firing threshold. (A1) Cell Rin was systematically measured using positive current steps generating 5–10-mV subthreshold depolarizations. The voltage shifts (ΔVm) and currents steps (ΔI) to define the average Rin in the cell are illustrated in red. (A2) Histograms and box plots present Rin in pvalb neurons in humans (blue) and mice (gray). The bin is 25 MΩ, and box plots present the median, quartiles, and 5th and 95th percentiles (Mann–Whitney U-test).

(B) pvalb cells exhibit a longer tau in humans than in mice for Vm changes in the soma. (B1) Tau was measured from the ascending phase in +10-mV steps delivered at −70 mV (human, blue; mouse, gray). Left: superimposed (four) +10-mV steps in human and mouse pvalb cells. Right: Ascending phase of the voltage steps displays differences in tau (average: 8.9 ms in humans and 3.4 ms in mice). (B2) Histograms and box plots illustrate the difference in tau between human (blue) and mouse (gray) pvalb neurons. Histogram bin, 0.5 ms (Mann–Whitney U-test).

(C) Membrane tau and Rin in the soma are tightly associated in mouse pvalb neurons (C1) but not in human pvalb neurons (C2; Spearman's correlation test).

(D) A low AP firing threshold is associated with slow membrane tau in mouse (D1) and human pvalb neurons (D2). (D3) Values from both species pooled together reveal a strong association between slow tau and a low AP firing threshold (Spearman's correlation test).

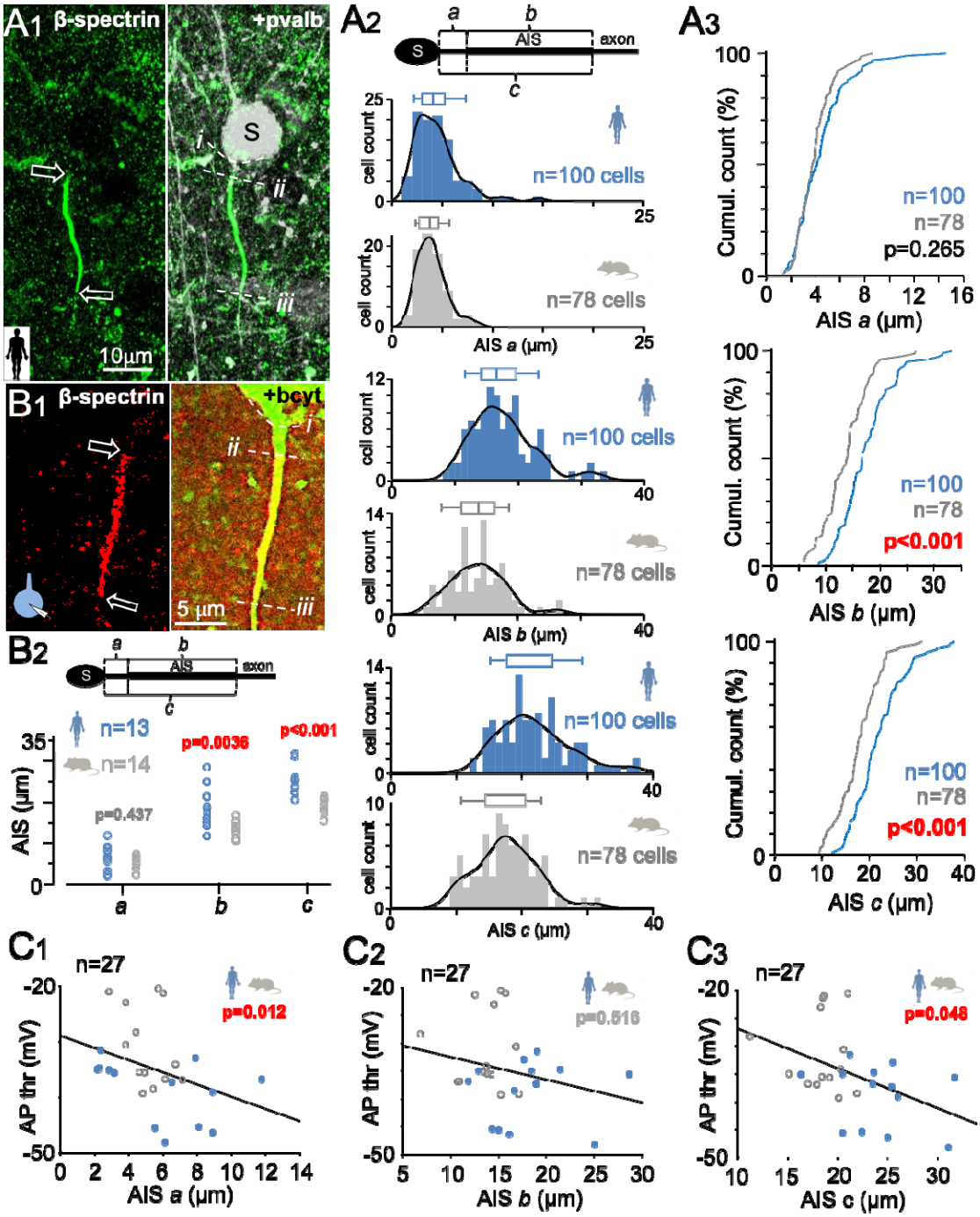

Fig. 3. The AIS is elongated in human pvalb neurons compared with that in mouse, and its location along the axon is associated with the AP threshold. (A) The AIS in pvalb neurons is longer in humans than in mice. Analysis of the AIS in triple-immunostained neurons in the human and mouse neocortex. (A1) The AIS was measured in three-dimensional fluorescence confocal microscopic images of human and mouse pvalb immunopositive neurons in layer 2/3. Left: The AIS was visualized via immunofluorescence for beta-IV-spectrin. Arrows denote the initiation and termination sites of the AIS (Alexa

488) in a collapsed z-stack image of human pvalb neuron. Right: Merged image of beta-IV-spectrin and pvalb (cy5) immunoreactions. Horizontal dotted curves denote (i) the axon from the soma (s) and the proximal (ii) and (iii) distal ends of the AIS. (A2) Histograms and box plots summarize three AIS parameters as defined in the upper schematic: a = distance from the soma to the AIS initiation site, b = AIS length, and c = distance from the soma to the end of the AIS. Top: distance from the soma to the AIS initiation site does not differ between the species. Middle: the AIS is longer in human neurons than in mouse neurons. Bottom: the termination site of the AIS is more distant in human neurons than in mouse neurons. The histogram bin is 1 µm with kernel density. Box plots present the median, quartiles, and 5th and 95th percentiles. (A3) The AIS data in cumulative histograms show p-values (Student's *t*-test).

(B–C) AIS measurement in electrophysiologically examined pvalb neurons reveals the association of a low AP firing threshold with the distal termination site of the AIS. (B1) The AIS was visualized via immunopositivity for beta-IV-spectrin (cy3) in human and mouse pvalb cells recorded in whole-cell and filled with biocytin (bcyt), and visualized with streptavidin–Alexa 488. Immunofluorescence images present the AIS with the parameters defined in *A1*. (B2) Electrophysiologically studied pvalb neurons display a longer AIS (*b*) with a more distally localized termination site (*c*) compared with the findings in mouse neurons, but the distance from the AIS initiation site (*a*) to the soma did not differ between the species (Mann–Whitney U-test). Combined AP threshold data from human (blue symbols) and mouse (gray) pvalb neurons reveal an association with the AIS initiation site distance (C1), no association with AIS length (C2), and association with (C3) the distance from the AIS termination site to the soma (Spearman's correlation test).

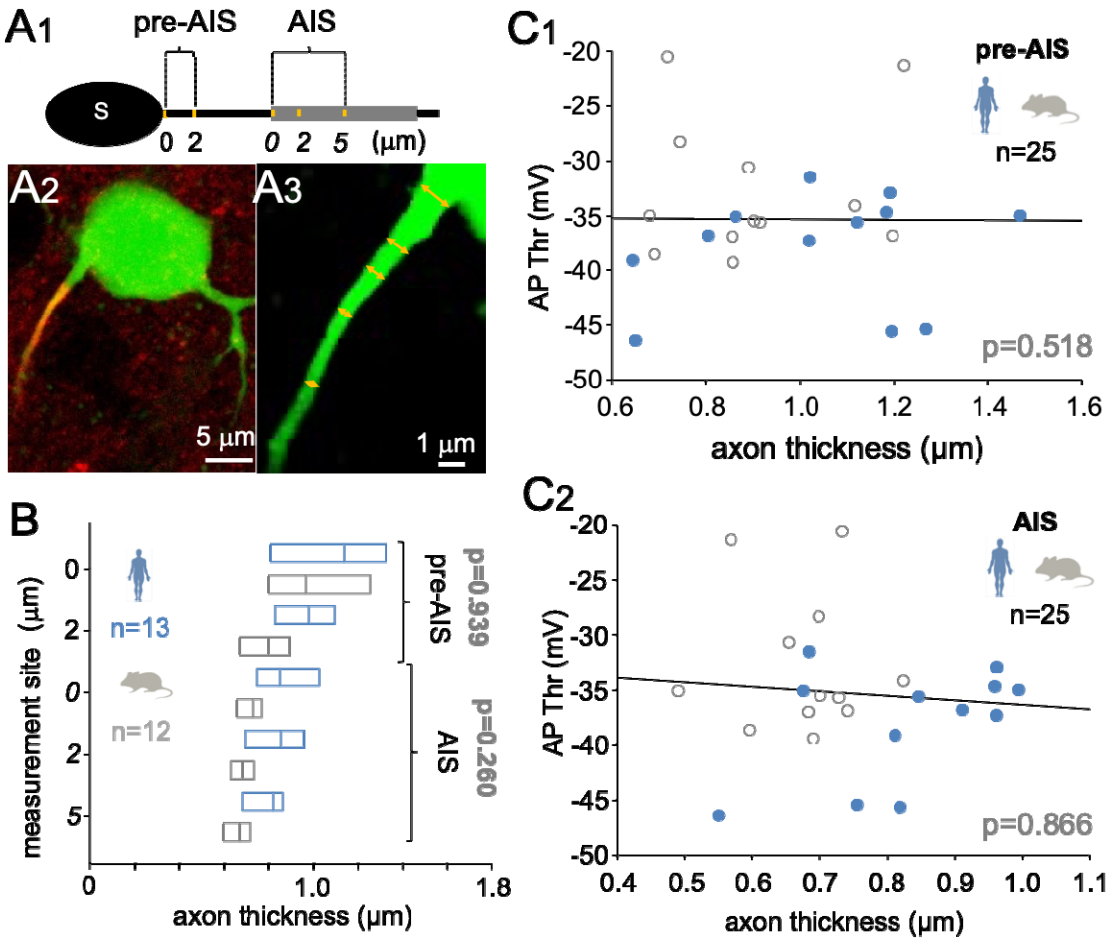

Fig. 4. The axon diameter fails to explain the interspecies difference in the AP firing threshold in pvalb interneurons. (A) Measurement of the axon cross-diameter in three-dimensional confocal microscopic images of biocytin-filled pvalb interneurons. (A1) Schematic presents the axon maximum width at five location sites of the axon. "pre-AIS" sites reflect measurement at the axon initiation point (shown as 0 µm from the soma) and 2 µm from soma. "AIS" sites represent measurement at the initiation point of the AIS (shown as *0*) and at *2* and *5* µm from the initiation site. (A2) Fluorescence confocal microscopic image (collapsed from the z-stack) presenting biocytin-filled pvalb neurons (Alexa 488) in humans with the AIS visualized by immunoreaction for beta-IV-spectrin (cy3). (A3) Zoom-in image of the axon with five measurement sites.

(B) Axon thickness did not differ between human (blue) and mouse (gray) pvalb neurons. Horizontal bars denote the median and quartiles.

(C) The axon diameter was not associated with the AP firing threshold in pvalb neurons in the pre-AIS area (C1) or AIS (C2). Data were pooled from both species (one-way ANOVA on ranks with Dunn's pairwise *post hoc* test).

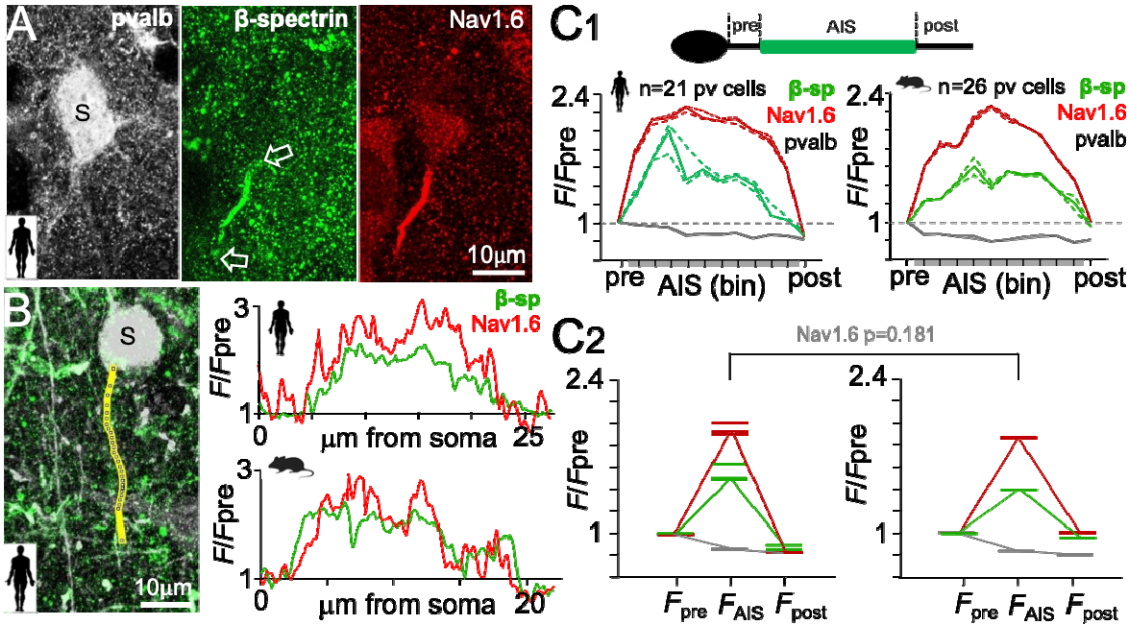

Fig. 5. The AIS displays similarly robust and uniform immunofluorescence for the low-voltage-activated Nav1.6 channel in human and mouse pvalb neurons. (A) The triple immunofluorescence reaction for pvalb (cy5), beta-IV-spectrin (Alexa 488), and Nav1.6 (cy3) uncovered the sodium channel localization pattern in the human pvalb neuron AIS. Collapsed z-stack confocal microscopic images. Arrows denote the AIS initiation and termination sites, s indicates the pvalb neuron soma.

(B) The immunofluorescence intensity was measured along the axon from its initiation site at the soma (s) beyond the termination site of the AIS in a confocal three-dimensional stack of images. Left: the measurement line along the axon of a pvalb neuron (the beta-IV-spectrin–visualized AIS is masked in the image by the measurement line). The picture is collapsed from z-stack images. Right, top: fluorescence intensity was measured along the three-dimensional pixel line for beta-IV-spectrin (green) and Nav1.6 (red). Right, bottom: similar measurement in a mouse pvalb neuron. The abscissa '0' indicates the axon initiation point from the soma. The vertical scales are normalized by the average of the "pre-AIS" values for each trace.

(C) The line analysis in human and mouse pvalb cells revealed a robust immunoreaction for Nav1.6 channels in the AIS. (C1) Traces indicate the median (solid line) and quartiles (dotted lines) of the immunofluorescence intensity along the axon. Lines are normalized by the pre-AIS average in each cell before pooling. The upper schematic denotes the definition of the AIS (by beta-IV-spectrin immunofluorescence) and the pre-AIS and post-AIS in the axon. The AIS length was divided to 10 bins in each cell. (C2) Median and quartiles of fluorescence intensity in the pre-AIS, AIS, and post-AIS parts of the axon in human (left) and mouse (right) pvalb cells. Values were normalized by the pre-AIS value for each measurement trace before pooling the data (Mann–Whitney U-test).

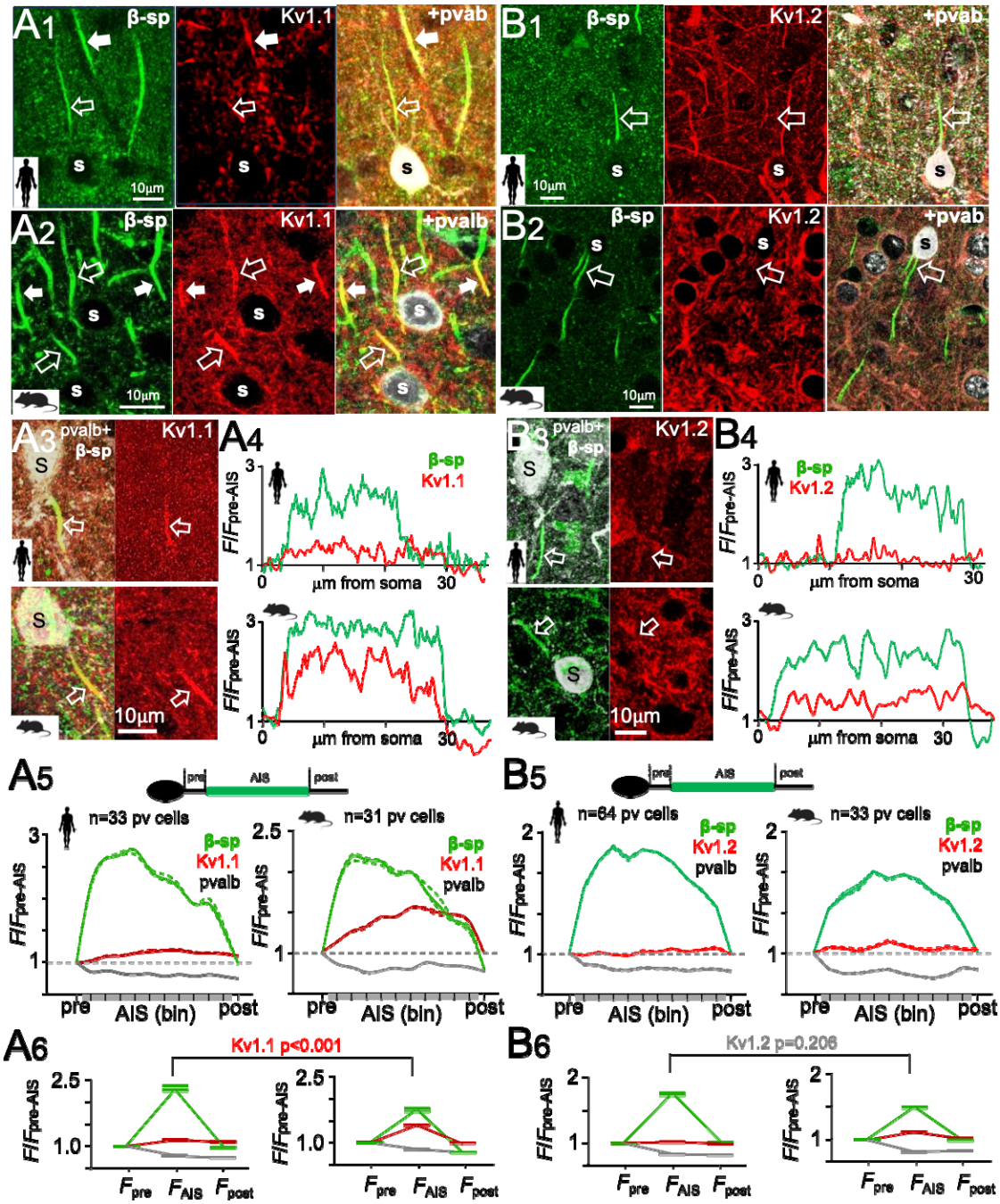

Fig. 6. The AIS is deficient in Kv1 potassium channels in humans compared with mice. (A) Immunofluorescence staining in pvalb neurons reveals a robust difference between humans and mice for Kv1.1 expression in the AIS. (A1) Triple immunofluorescence reaction for beta-IV-spectrin (β-sp, Alexa 488), Kv1.1 (cy3), and pvalb (cy5) in layer 2/3 in the human neocortex. Arrows denote AISs visualized using beta-IV-spectrin (left) and Kv1.1 (middle) in a pvalb+ (open arrow) neuron and a pvalb− (solid arrow) neuron (right, merged image with pvalb immunoreaction). S indicates the pvalb+ cell soma. The pvalb+ neuron lacks immunoreactivity for Kv1.1, although the AIS of the pvalb− neuron exhibited a robust Kv1.1 signal. (A2) Triple immunofluorescence reaction for beta-IV-spectrin (β-sp, Alexa

488), Kv1.1 (cy3), and pvalb (cy5) in layer 2/3 in the mouse neocortex. Open and solid arrows denote the AISs of pvalb+ and pvalb− neurons, respectively. Kv1.1 immunoreactivity is robust in the AISs of both pvalb+ and pvalb− neurons in mice. (A3) Top: Zoomed-in image of detectable immunoreactivity for Kv1.1 in the human pvalb+ neuron AIS. Bottom: Typical AIS pvalb+ neuron immunoreaction in mice. Open arrow denotes the AIS. (A4) Immunofluorescence line analysis of axons in the human (top) and mouse (bottom) neurons for beta-IV-spectrin (green line) and Kv1.1 (red line; traces normalized by the intensity average in the axon preceding the AIS). (A5–6). The line analysis in several human and mouse pvalb cells reveals weak immunofluorescence for Kv1.1 in the human AIS but robust immunofluorescence in the mouse AIS. (A5) Median (solid line) and quartiles (dotted lines) of fluorescence intensity of the traces normalized by the pre-AIS average. The schematic presents the definitions of the AIS (by beta-IV-spectrin positivity), pre-AIS, and post-AIS in the axon. (A6) Median and quartiles of fluorescence intensity in the pre-AIS, AIS, and post-AIS of the axon in human (left) and mouse (right) pvalb cells (Mann–Whitney U-test).

(B) Immunofluorescence staining for Kv1.2 was equally weak in the AIS in human and mouse pvalb neurons. (B1) Triple immunofluorescence staining for beta-IV-spectrin (β-sp, Alexa 488), Kv1.2 (cy3), and pvalb (cy5) in humans and mice (B2). Arrows denote the AIS visualized by beta-IV-spectrin immunoreactivity (left) but lacking Kv1.2 immunoreactivity (middle) in pvalb+ neurons (right, merged image with pvalb immunoreactivity), although the Kv1.2 reaction was robust in the soma and dendrites. S; pvalb+ cell soma. (B3) Zoomed-in image of triple immunoreaction in human pvalb+ neurons with human- (top) and mouse-type AISs (bottom). The open arrows denote the AIS. (B4) Immunofluorescence intensity line analysis of axons in human (top) and mouse (bottom) neurons for beta-IV-spectrin (green line) and Kv1.2 (red line; normalized by the intensity average of the pre-AIS). (B5–6). The line analysis in various pvalb neurons in humans and mice presents the weakness of immunofluorescence signal for Kv1.2 in the AIS. (B5) Median (solid line) and quartiles (dotted lines) of fluorescence intensity of traces normalized by the pre-AIS average. (B6) Median and quartiles of the fluorescence intensity in the pre-AIS, the AIS, and post-AIS in human (left) and mouse (right) pvalb neurons (Mann–Whitney U-test).

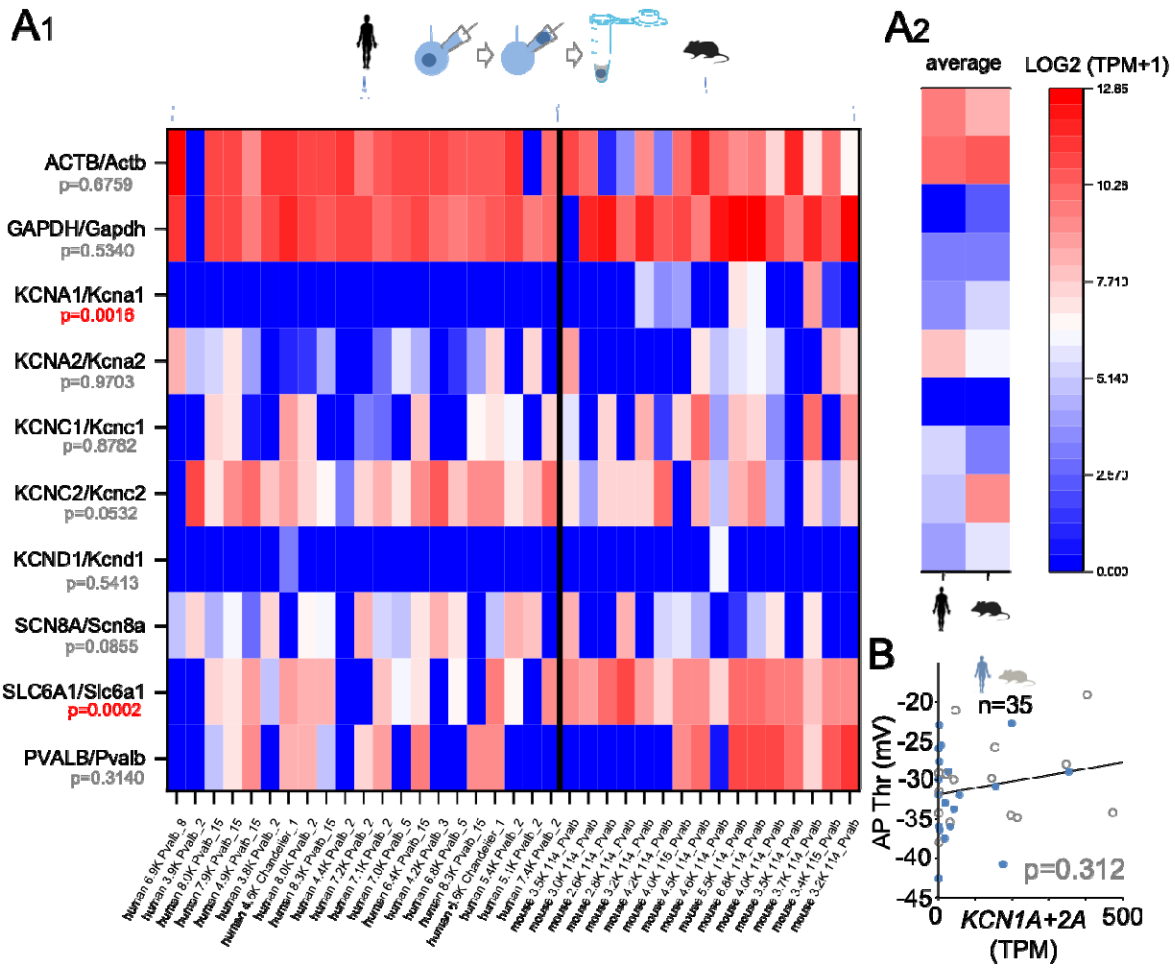

Fig. 7. Human pvalb neurons lack mRNA for *KCNA1* encoding Kv1.1 channels, but mice and humans have equal *KCNA2* mRNA levels. (A) mRNA analysis of patch-sequenced human and mouse pvalb neurons (upper schematic illustrates the protocol) revealed the absence of *KCNA1* expression in all human neurons, whereas it was robustly expressed in many mouse cells. (A1) Heatmap presents the mRNA levels (TPM) in individual human (n = 21) and mouse (n = 16) pvalb neurons for genes encoding low-threshold channels in the AIS, as well as housekeeping genes *GAPDH* and *ACTB*. Human and mouse cells differ quantitatively (TPM values) and categorically (positive or negative gene expression) regarding the expression of *KCNA1* (*90*), but no difference was observed for the other ion channel genes. Similar *KCNA2*, *KCNC1*, and *KCNC2* expression was observed in both species (*61*), and *KCND1* was virtually not expressed in either human or mouse cells (*62*). In addition, *SCN8A* encoding Nav1.6 channels and *SLC6A1* encoding GABA transporter type-1 were abundant in both species. Human and mouse cells also exhibited different mRNA expression of *SCL6A1* encoding GABA transporter 1. Significant p-values comparing TPM values are presented in red (with genes, ordinate). The code for each pvalb cell subtype, as identified by the gene expression profile of the Allen Institute database, is presented at the bottom of the heatmap (see also Fig. S1). (A2) Averaged TMP values for the same genes (ordinate) in human (n = 21) and mouse (n = 16) cells.

(B) There was no association of the pooled mRNA levels (TPM) of *KCNA1* and *KCNA2* with the AP threshold (human, blue symbols; mouse gray symbols) (Spearman's correlation test).

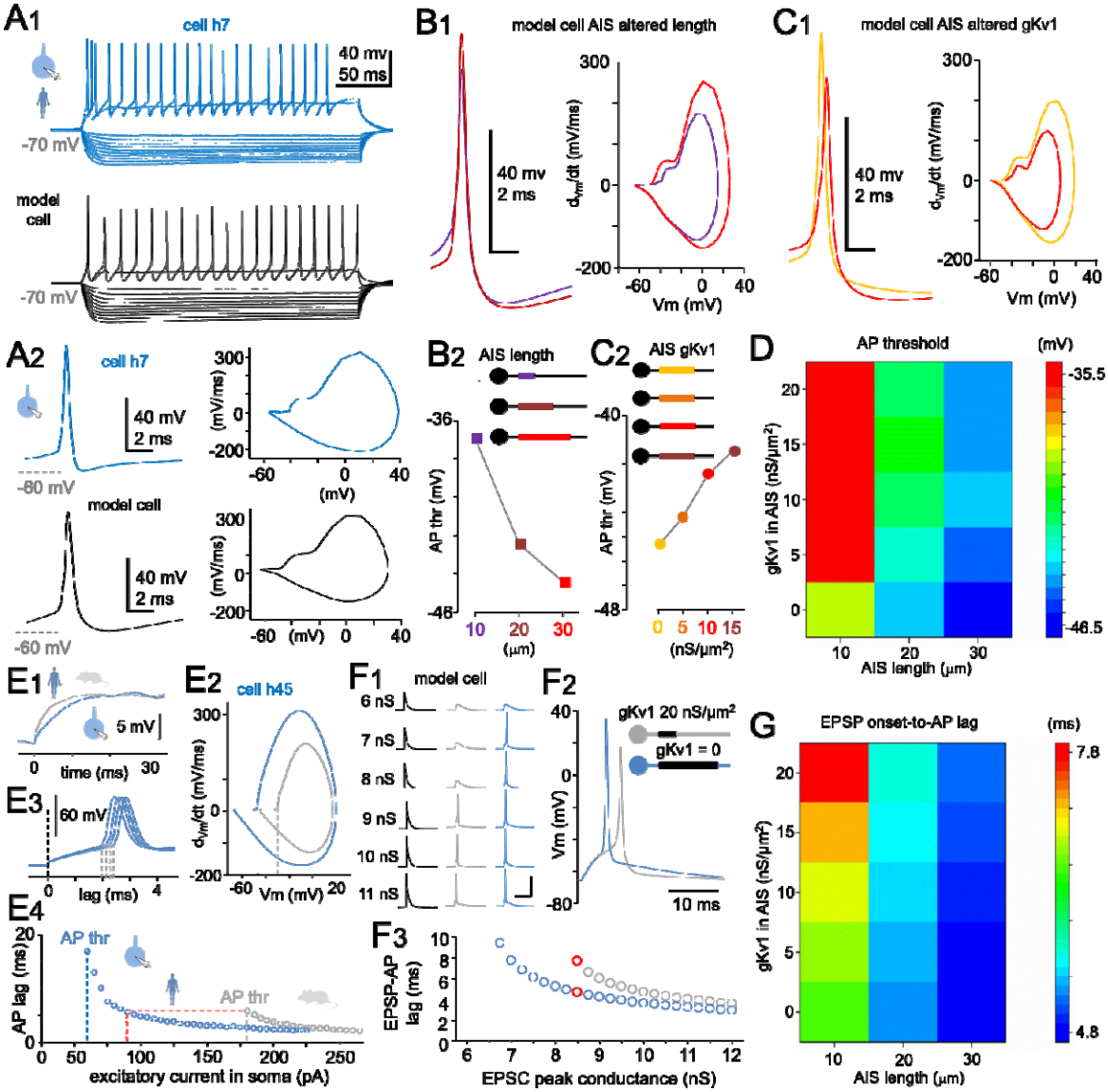

Fig. 8. The fast-spiking neuron computational model illustrated that the human-type AIS lowers the AP firing threshold and shortens the AP generation lag to excitation in the soma. (A) A computational single-cell model with axon and dendrite cable properties replicates the human pvalb cell electrical activity measured in the soma. (A1) Vm responses in human pvalb neurons in the whole-cell recording (real-life cell, blue) and the model cell (gray) by current steps from −200 to +200 pA. (A2) Left: AP (first AP elicited by the lowest suprathreshold step) in a real-life neuron (blue) and the model cell (gray). Right: phase plots of the APs.

(B) Lengthening of the AIS from 10 to 30 µm, a range observed in real-life pvalb cells, efficiently lowered the AP firing threshold in the model cell (Kv1 and Nav1.6 channel activity = 20 nS/µm^2; distance from the AIS initiation site to the soma = 10 µm; axon Ra = 0.9 MΩ·µm: axon diameter = 0.8 µm). (B1) Model cell APs and the phase plots with AIS lengths of 10 (purple) and 30 µm (red). (B2) AP firing threshold simulated with three

different AIS lengths, namely 10 (purple), 20 (brown), and 30 µm (red), as illustrated in the schematic inset. The firing threshold was particularly sensitive to an AIS length of 10–20 µm, a range observed in most real-life human and mouse pvalb neurons.

(C) Reduced Kv1 potassium channel activity in the AIS lowers the AP firing threshold in the model neuron. (C1) AP and phase plot generated with different Kv1 channel activities in the AIS. (C1) AP and its phase plot with gKv1of 0 (yellow) and 15 nS/µm^2 (red) in the AIS. (C2) The AP firing threshold with different Kv1 activities (gKv1 = 0, 5, 10, and 15 nS/µm^2, abscissa) in the AIS (Nav1.6 channel activity = 20 nS/µm^2; AIS length = 20 µm; distance from the AIS initiate site to the soma = 10 µm).

(D) The combination of an elongated AIS and reduced Kv1 activity effectively lowered the AP threshold in the model neuron. The heatmap illustrates the combined effect of Kv1 activity (gKv1 density in the AIS extracellular membrane in the ordinate) and AIS length (abscissa) on the AP firing threshold. The difference between the minimum and maximum simulated AP threshold was 11 mV. The calibration for color-coded AP threshold (Vm) is presented on the right.

(E–G) Shortening of the AP generation lag by the human-type AIS. **(E)** Sample real-life neurons in human and mouse with different membrane depolarization kinetics and AP thresholds but a similarly short AP generation time lag. The human pvalb neuron (blue) had a slower membrane depolarization (E1) and lower AP threshold (E2) than the mouse pvalb neuron (gray). (E3) AP generation lag (to the depolarizing step in the soma) from the depolarizing step onset (black dotted lines) to the AP onset (gray dotted line) presented in the four sample traces (AP onset defined as a rise speed of 10 mV/ms). (E4) AP generation lag in human (blue symbols) and mouse (gray symbols) neurons by the excitatory current steps in the soma. The human pvalb neuron triggered AP with a smaller current intensity than the mouse neuron (abscissa, AP threshold current intensity denoted by the dotted vertical lines). The human neuron generated AP with a similar time lag (indicated by the dotted horizontal line) as the mouse cell with a lower excitatory current intensity.

(F) Changing the model neuron AIS properties from mouse-like to human-like shortened the AP generation time lag to the fixed-strength excitation in the soma. (F1) The human-type AIS lowered the AP threshold to the EPSC simulated in the model neuron soma. Vm traces presenting the EPSP of incremental strength eventually triggering an AP in the model neuron with human (blue) and mouse (gray) AISs. The EPSP-generating conductance of the incremental peak amplitude from 6 to 11 nS is presented on the left (black traces). Scale: 40 ms and 50 mV. (F2) The human-type AIS shortened the AP generation time lag by EPSP in the soma. Traces present EPSPs with AP generated with human-type (blue) or mouse-type (gray) with equal-strength EPSC (8.5 nS peak conductance) in the soma. (F3) Plot presents the AP generation time lag in the model cell to incremental EPSC strength increases in the model cell with human-type (blue dots) and mouse-type (gray dots) AISs. Responses to EPSC conductance of 8.5 nS is presented in red.

(G) Heatmap presenting the combined effect of AIS length (abscissa) and AIS Kv1 activity (ordinate) on the AP generation time lag by fixed-strength EPSC (8.5 nS) in the model neuron. Calibration for color-coded time lag (ms) is shown on the right.

Supplementary Materials

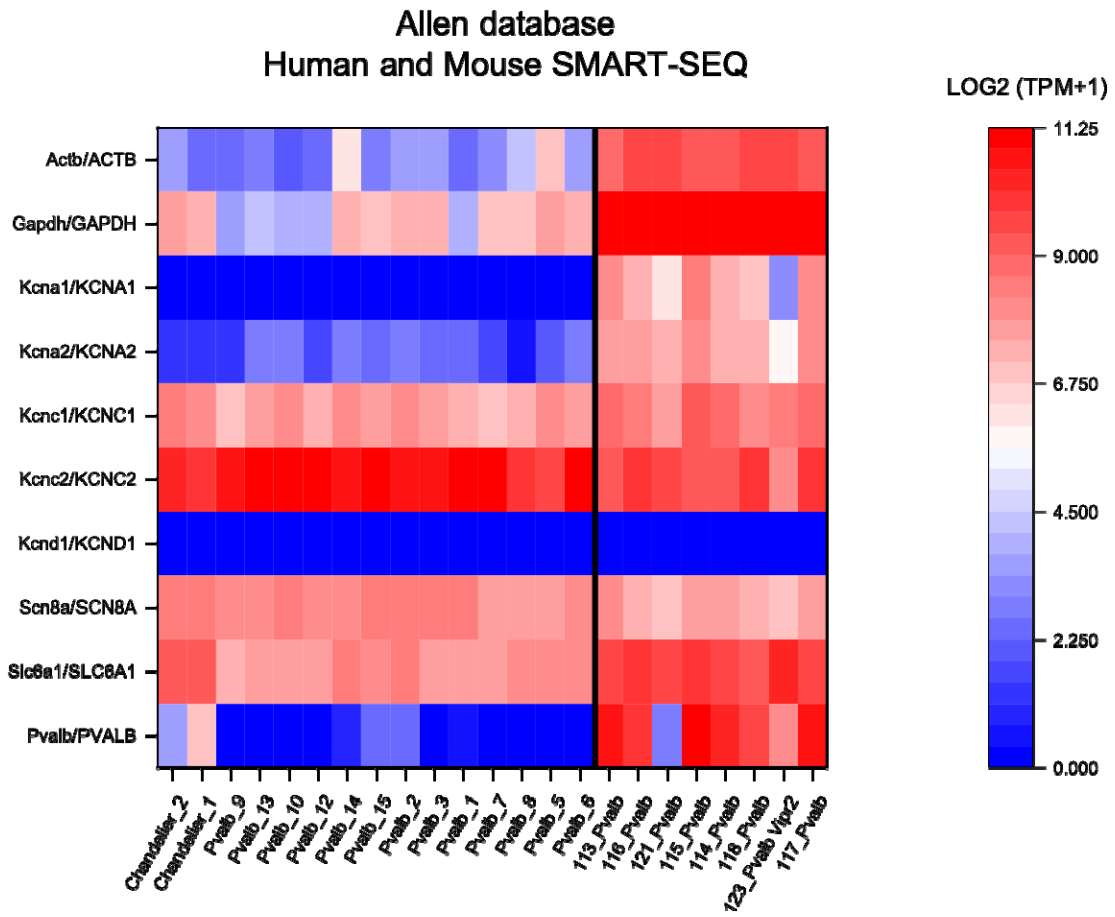

Fig. S1. The Allen Institute database on pvalb interneuron subtypes in the human neocortex layer 2/3 revealed a deficiency of *KCNA1* mRNA in the human cells.

The heatmap presents the TPM values (scaling on right) of the average values in seven human and eight mouse pvalb neuron subtypes in layer 2/3 in the neocortex as identified by the dataset. Significant differences in *KCNA1* TPM values were detected (one-way MANOVA with Bonferroni's *post hoc* test), and differences were noted when tested categorically (expressed vs. not expressed, chi-squared test after Benjamini–Hochberg adjustment at the 5% significance level; $p = 0.0011$ and $p < 0.001$, respectively). The abscissa lists the pvalb cell subtypes (as also used in Fig. 7).

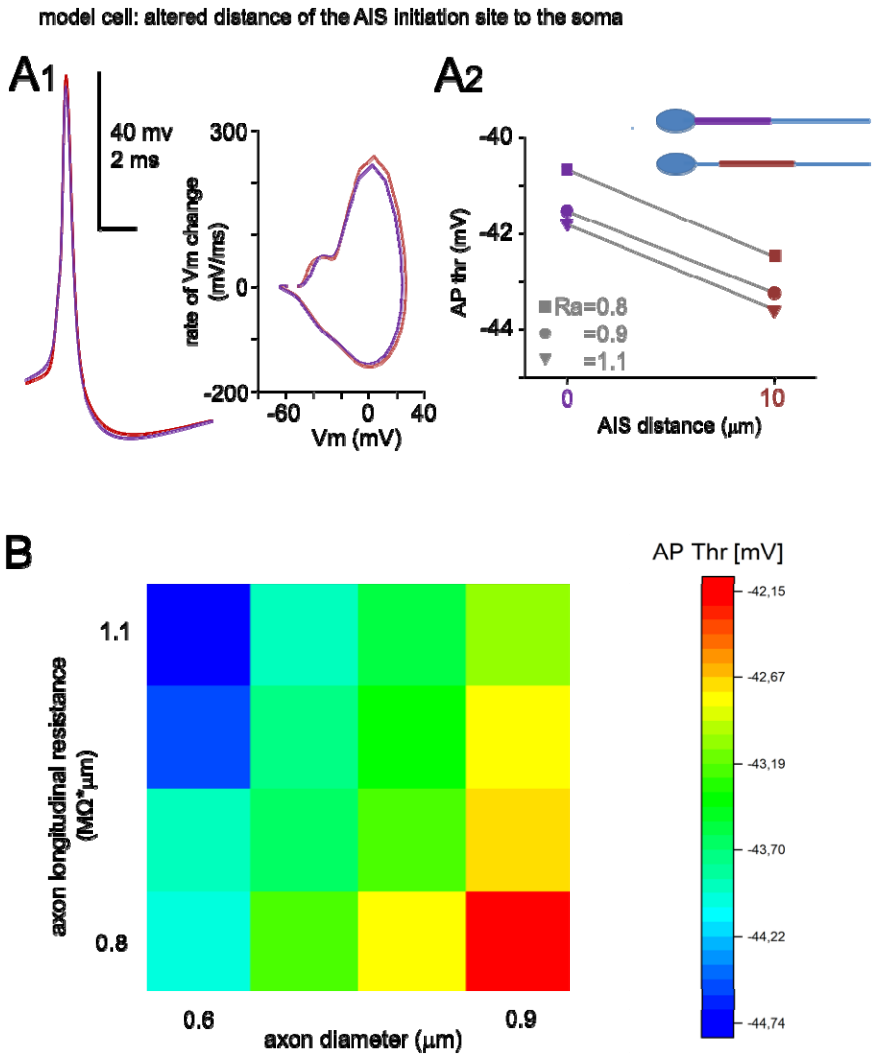

Fig. S2. Model cell simulation with the AIS properties exhibiting cell-to-cell variability but no difference between humans and mice.

(A) The location of the AIS in the proximal–distal axis along the axon over a range observed in an anatomical study regulated the AP firing threshold. The AP generation firing threshold was simulated in the model cell with excitatory Vm changes (incremental amplitude square-pulse current steps), similar to the experiments in Figure 8. (A1) Traces of AP generated by simulation in the model cell with the AIS (20 µm in length, axon Ra = 0.8–1.1 MΩ·µm, axon diameter = 0.8 µm, channel activity = 20 nS/µm^2 for both Nav1.6 and Kv1) initiating immediately in the beginning of axon (distance to soma = 0 µm; purple) or 10 µm from the soma (brown). (A2) Plot presents the firing threshold for APs simulated with the two localizations of the AIS along the axon. The simulation was run with three alternative Ra values of the axon (0.8–1.1 MΩ·µm as denoted by different symbols). The simulation revealed a similar result with the three Ra values in that a more distal AIS initiation site allowed a more negative AP firing threshold. The simulation result was in line with our observation in Fig. 3C1 illustrating a similar correlation between these two parameters in real-life pvalb neurons.

(B) The heatmap presents the relationship of the two parameters, which changed concurrently in a real-life situation but were altered separately in the model. The model simulated a 1.3-

fold increase in the Kv1 and Nav1.6 ion channel activities in the AIS with any increase in the axon diameter.

cell code	pvalb+ or mRNA	APThr	gender	age (years)	hemisphere	region	diagnosis
h1	pvalb+	-42	F	69	right	occipital	subcortical neoplasia

1451

h2	pvalb+	-37,3	M	38	right	temporal	malformation
h3	pvalb+	-46,8	M	38	right	temporal	malformation
h4	pvalb+	-38,5	M	66	right	temporal	tumor
h5	pvalb+	-40,1	M	45	left	frontal	tumor
h6	pvalb+	-48,2	M	21	right	parietal	tumor
h7	pvalb+	-39,1	M	21	right	parietal	tumor
h8	pvalb+	-32,9	M	40	right	frontal	tumor
h9	pvalb+	-45,6	F	70	left	parietal	hydrocephalus
h10	pvalb+	-40,2	M	69	right	parietal	hydrocephalus
h11	pvalb+	-36,8	M	58	right	frontal	tumor
h12	pvalb+	-46,1	M	58	right	frontal	tumor
h13	pvalb+	-47	F	66	right	frontal	tumor
h14	pvalb+	-26,6	F	21	right	frontal	hydrocephalus
h15	pvalb+	-27,5	no info	no info	left	parietal	tumor
h16	pvalb+	-35	F	72	right	temporobasal	tumor
h17	pvalb+	-41,3	F	72	right	temporobasal	tumor
h18	pvalb+	-46,4	M	47	left	frontotemporal	tumor
h19	pvalb+	-34,7	M	38	right	temporal	malformation
h20	pvalb+	-38,8	M	38	right	temporal	malformation
h21	pvalb+	-45,4	M	34	left	cerebellar	malformation
h22	pvalb+	-49,1	M	11	left	temporal	malformation
h23	pvalb+	-40,5	F	61	right	frontal	tumor
h24	pvalb+	-27,9	F	17	right	parietal	tumor
h25	pvalb+	-31,2	F	65	right	frontal	colloid cysta
h26	pvalb+	-30,6	M	85	left	fronto-temporal	hydrocephalus
h27	pvalb+	-37,6	F	28	right	temporal	hydrocephalus
h28	pvalb+	-37	F	30	no info	no info	hydrocephalus
h29	pvalb+	-39,9	F	40	right	frontal	anaplastic ependymoma
h30	pvalb+	-36,8	F	40	right	frontal	anaplastic ependymoma
h31	pvalb+	-35,6	F	42	left	fronto-temporal	astrocytoma
h32	pvalb+	-39	F	78	right	frontal	hydrocephalus
h33	pvalb+	-41,1	F	68	right	temporal	hydrocephalus
h34	pvalb+	-49	F	68	right	temporal	hydrocephalus
h35	pvalb+	-38,9	F	19	right	frontal	subcortical neoplasia
h36	pvalb+	-55,8	F	19	right	frontal	subcortical neoplasia
h37	pvalb+	-52	F	50	left	occipital	astrocytoma
h38	pvalb+	-20,1	F	54	right	frontal	aneurysm
h39	pvalb+	-53,1	F	69	no info	no info	hydrocephalus
h40	pvalb+	-25,5	M	36	right	frontal	hydrocephalus
h41	pvalb+	-30	M	37	right	parietal	tumor
h42	pvalb+	-48,7	F	60	right	parietal	hydrocephalus
h43	pvalb+	-31	M	22	right	frontal	hydrocephalus
h44	pvalb+	-40,7	F	39	right	frontal	tumor
h45	pvalb+	-47,7	F	63	right	temporal	hydrocephalus
h46	pvalb+	-52,6	F	68	right	temporal	hydrocephalus
h47	pvalb+	-42,2	F	76	right	frontal	Hydrocephalus

h48	pvalb+	-41,1	F	73	right	frontal	biopsy (MRI: multifocal lesions)
h49	pvalb+	-40,9	F	73	right	frontal	biopsy (MRI: multifocal lesions)
h50	pvalb+	-54	M	33	right	frontal	hydrocephalus
h51	pvalb+	-39	M	20	right	frontal	hydrocephalus
h52	pvalb+	-42,7	M	49	right	frontal	colloid cyst
h53	pvalb+	-47,6	M	66	right	frontal	astrocytoma
h54	pvalb+	-36,2	M	67	right	occipital	subcortical neoplasia
h55	pvalb+	-53,3	M	68	no info	temporal	hydrocephalus
h56	pvalb+	-45,5	M	51	no info	no info	hydrocephalus
h57	pvalb+	-38,4	F	47	right	frontal	colloid cyst
h58	pvalb+	-38,4	F	53	left	no info	tumor
h59	pvalb+	-45,9	F	30	right	frontal	tumor
h60	pvalb+	-36,4	F	30	right	frontal	tumor
h61	pvalb+	-34,8	M	41	right	parietal	shunt
h62	pvalb+	-32,3	M	20	right	temporal	tumor
h63	pvalb+	-37,7	M	43	right	frontal	tumor
h64	pvalb+	-37	M	65	right	temporal	tumor
h65	pvalb+	-35	M	65	right	temporal	tumor
h66	pvalb+	-38,5	F	67	right	parietal	shunt
h67	pvalb+	-40,6	F	55	left	temporal	tumor
h68	pvalb+	-39,3	F	79	right	parietal	hydrocephalus
h69	mRNA	-31,9	F	51	right	Insula	tumor
h70	mRNA	-25,5	M	no info	right	frontal	tumor
h71	mRNA	-42,8	M	no info	right	frontal	tumor
h72	mRNA	-28,9	M	no info	right	frontal	tumor
h73	mRNA	-26,6	M	no info	right	frontal	tumor
h74	mRNA	-21,9	M	no info	right	frontal	tumor
h75	mRNA	-32,8	M	70	left	temporal	cavernoma
h76	mRNA	-37,6	F	51	right	Insula	tumor
h77	mRNA	-31,1	F	51	right	insula	tumor
h78	mRNA	-33,9	F	51	right	insula	tumor
h79	mRNA	-40,5	M	no info	left	frontal	hydrocephalus
h80	mRNA	-32,8	M	59	right	frontal	tumor

Table S1. List of pvalb cells in the human neocortex in the study.